Experimental study of the flow in the wake of a stationary sphere immersed in a turbulent boundary layer

René van Hout,[1,*] Jerke Eisma,[2] Gerrit E. Elsinga,[2] and Jerry Westerweel[2,†]
[1]*Technion–Israel Institute of Technology, Technion city, Haifa, Israel*
[2]*TU-Delft, 3ME Aero- and Hydrodynamics Laboratory, Leeghwaterstraat 21, 2628 CA, Delft, The Netherlands*

(Received 16 October 2017; published 2 February 2018)

In many applications, finite-sized particles are immersed in a turbulent boundary layer (TBL) and it is of interest to study wall effects on the instantaneous shedding of turbulence structures and associated mean velocity and Reynolds stress distributions. Here, 3D flow field dynamics in the wake of a prototypical, small sphere ($D^+ = 50$, $692 < \mathrm{Re}_D < 959$) placed in the TBL's outer, logarithmic, and buffer layer, were measured using time-resolved tomo-PIV. Increasing wall proximity increasingly tilted the mean recirculating wake away from the wall implying a negative lift force. Mean velocity deficit recovery scaled with the mean wake length with minor effects of wall proximity. Farthest from the wall, streamwise Reynolds normal stresses encircled the mean wake as an axisymmetric tubular "shell," while transverse and wall-normal stresses extended off its tip as axisymmetric tapered cones. Wall proximity removed axisymmetry and attenuated values near the wall. Reynolds shear stresses were distributed as antisymmetric lobes extending off the mean wake displaying increasing values with reducing sphere-wall gap. Instantaneous snapshots revealed a wake densely populated by "archlike" vortices with shedding frequencies lower than for a sphere in uniform flow except in the buffer layer. Tilting of the wake away from the wall resulted from self-induced motion of shed hairpinlike vortices whose symmetry plane was increasingly wall-normal oriented with reduced sphere-wall gap.

DOI: 10.1103/PhysRevFluids.3.024601

I. INTRODUCTION

Turbulent flows around finite-sized particles are encountered in many environmental applications, such as pebbles or large droplets in aquatic and atmospheric environments. When these particles are suspended in turbulent flows they interact with the flow in an intricate manner, and as a result they may enhance or suppress turbulence [1–8]. This enhancement or suppression has been coined two-way coupling in contrast to one-way coupling that describes particle advection by the flow without the particles affecting the flow of the carrier fluid. The flow around finite-sized particles is characterized by a downstream wake that may be steady or unsteady depending on the Reynolds number, $\mathrm{Re}_D = U_c D/\nu$, where U_c denotes the undisturbed velocity at the position of the sphere center, D the sphere diameter, and ν the fluid kinematic viscosity. One of the ways that particles can enhance turbulence is by vortex shedding [1] and/or wake oscillation in response to freestream turbulence [6,9].

Spheres are prototypical particles and many experiments and numerical simulations have studied the flow in the wake behind a sphere in a uniform flow over a wide Reynolds number range [10–18]. These studies indicated that vortex shedding is initiated when Re_D equals about 270 [13,15]. Initially,

*rene@technion.ac.il
†J.Westerweel@tudelft.nl

vortex shedding is highly organized and characterized by well-ordered sequences of connected hairpin vortices with alternating orientation of their "heads" [15]. However, when Re_D exceeds 800 the large vortices disintegrate into smaller ones as a result of shear layer instabilities [13], and the normalized vortex shedding frequency, f_s, given by the Strouhal number, $\mathrm{St}_D = f_s D/U_c$, displays both low- and high-frequency branches [19].

The effect of free stream turbulence on the wake of a sphere as well as on the drag force has been studied experimentally [20–23] as well as numerically [9,24]. These studies showed that the mean velocity deficit in the far wake of the sphere displayed self-similarity, similar as in nonturbulent ambient conditions. Wu and Faeth [20] showed that neither the onset of vortex shedding nor its frequency was affected by free stream turbulence intensity up to 4% ($135 < \mathrm{Re}_D < 1560$). Amoura *et al.* [23] measured the mean flow and turbulence characteristics in the wake of a sphere exposed to intense incident turbulence (turbulence intensity up to 45%) characterized by an integral length scale of the order of D. Their results indicated that the mean velocity deficit along the sphere's axis is successively controlled by the mean (inside the recirculating wake) and the incident fluctuating velocities (downstream of the recirculating wake). Furthermore, their results suggested that at a given turbulence intensity (26%), the mean recirculating wake length is independent of Re_D. Direct numerical simulations (DNS) by Bagchi and Balachandar [24] showed that the standard drag relation not including added mass and history effects well predicted the mean drag force irrespective of the free stream turbulence intensity (ranging from 10% to 25%). However, the accuracy of predicting the instantaneous drag diminished with increasing D. None of the above cases studied wall effects.

Since in many applications 3D bluff bodies reside in the vicinity of walls, it is of particular interest to investigate the effect of shear rate and boundary layer turbulence on the forces acting on a sphere and associated sphere shedding patterns [6,25–27]. Ozgoren *et al.* [27] measured the effect of reducing gap size on the wake of a sphere ($D/\delta = 0.67$, where δ denotes the TBL thickness) using planar particle image velocimetry (PIV). Zeng *et al.* [6,25] performed DNS on small spheres ($D \ll \delta$) with diameters ranging from $D^+ = 3.5$ to 25, where the superscript "+" denotes inner scaling in wall units, i.e., normalization by ν and the friction velocity u_τ. The spheres were positioned in the buffer layer ($42 \leqslant \mathrm{Re}_D \leqslant 295$) and at the center ($\mathrm{Re}_D = 325$ and 455) of a turbulent channel flow. Note that their maximum Reynolds number in the buffer layer was $\mathrm{Re}_D = 295$, i.e., just beyond the critical Reynolds number for vortex shedding, and only at this Re_D continuous vortex shedding was observed. Vortex shedding enhanced the turbulent kinetic energy while small spheres (no vortex shedding) located in the buffer layer suppressed turbulence. Furthermore, as a result of ambient turbulence, the length of the mean recirculating wake was reduced compared to a sphere positioned in a nonturbulent ambient flow. Both Zeng *et al.* [6] and Ozgoren *et al.* [27] observed that with decreasing distance from the wall, the sphere wake tilted away from the wall in contrast to a sphere in a laminar boundary flow for which the wake tilts towards the wall. Zeng *et al.* [6] suggested that the reduced pressure due to the higher velocity above the particle caused upward tilting. Zeng *et al.* [25] used existing correlations to predict drag and lift forces and showed that the instantaneous forcing on the spheres was well correlated with the passage of near-wall coherent turbulence structures. The time averaged lift force acting on particles in the buffer layer was small but always directed towards the wall (negative lift) in agreement with tilting of the wake away from the wall. Note that this is in contrast with particles attached to the wall within the viscous sublayer for which large positive lift forces were measured [28–30]. As far as the authors know, there are no measurements of the lift force acting on a particle placed in the buffer layer of a turbulent boundary. The effect of linear shear flow has been studied in the DNS by Zeng *et al.* [31] who found that for sphere to wall distances exceeding $0.75D$, the lift force became wall ward directed beyond a certain Reynolds number (see also Ref. [32]).

Due to experimental difficulties, few attempts have been made to quantitatively measure the instantaneous three-dimensional structure of the sphere wake while DNS studies have been limited to relatively low Re_D ($\leqslant 600$ [9,25]). Notable exceptions are those by Brücker [17] and Doh *et al.* [33] who studied the sphere wake in a uniform flow. The latter used 3D particle tracking velocimetry at $\mathrm{Re}_D = 1130$, while the former performed high-speed, 2D PIV measurements in a transverse plane

positioned in the near-wake of a stationary held sphere at $\mathrm{Re}_D = 500$ and 700 to reconstruct the spatiotemporal evolution of the streamwise vorticity. While Doh *et al.* [33] provided some snapshots of the instantaneous vorticity structure in the near wake of the sphere, Brücker [17] showed that ordered sequences of three or four double-sided, oppositely oriented hairpin vortices ("regular shedding") were interrupted by periods without any clear shedding. To the best of our knowledge, no quantitative 3D measurements have been published on the sphere wake in a turbulent (boundary layer) flow that allow to link the instantaneously shed vortices to the forces on the body as well as the mean flow and turbulence characteristics. Furthermore, while the DNS study by Zeng *et al.* [6] provided much insight on turbulence modulation of spheres much smaller than the boundary layer thickness and positioned near the wall, it was limited in Reynolds number range ($\mathrm{Re}_D \leqslant 295$), and continuous vortex shedding was only observed at the largest Re_D.

The present study is similar to the DNS by Zeng *et al.* [6,25], but it extends the Reynolds number range beyond $\mathrm{Re}_D = 600$ for which continuous vortex shedding governs and turbulent viscosity based models perform poorly. The goal is to measure the evolving, instantaneous 3D flow structure just downstream of a stationary held sphere ($D^+ = 50$) immersed subsequently in the buffer layer, the start of the log layer, and the outer layer of a near-zero pressure gradient turbulent boundary layer (TBL), thus allowing us to assess the effect of the wall position. The latter is shown to affect the orientation of the shed vortical structures, which helps to explain the measured averaged turbulence statistics such as Reynolds stress distributions and the development of the wake upon approaching the wall. Furthermore, it allows study of the interaction with TBL structures, or alternatively the development of typical TBL structures, e.g., hairpin vortices, from the wake structures. The measurements were performed using temporally resolved tomographic particle image velocimetry (tomo-PIV) that enabled us to capture the evolving 3D wake flow. First, the experimental setup and data processing are described in Sec. II. Mean velocity profiles and Reynolds shear stress profiles of the fully developed TBL without the sphere are presented in Sec. III and validated against literature results. The instantaneous vortical structure in the wake of the sphere is presented in Sec. IV, while in Sec. V the 3D distribution of the mean velocities and Reynolds stresses is discussed. In Sec. VI, the instantaneous flow structures in the wake of the sphere and, in particular, their orientation as a result of wall proximity are examined. Finally, Sec. VII presents the conclusions.

II. EXPERIMENTAL SETUP AND METHODOLOGY

Experiments were performed in the closed-loop water flume at the Laboratory for Aero- and Hydrodynamics at the Delft University of Technology, which in part is schematically depicted in Fig. 1. The cross-sectional area of the water that filled the flume was $60 \times 60\,\mathrm{cm}^2$. Measurements were performed in the boundary layer that was formed on the vertical channel side-wall made of 32-mm-thick transparent Plexiglas [Fig. 1(b)], which allowed good optical access. To force transition to turbulence, a zigzag strip [34] was placed 500 mm downstream of the inlet of the test section [Fig. 1(a)]. We used a tomographic PIV setup that makes it possible to measure all three instantaneous velocity components in a volumetric domain [35,36]. The tomo-PIV setup that is schematically shown in Fig. 1(b) comprised four high-speed cameras (ImagerPro, 2016×2016 pixels), a high-speed laser (Nd:YLF, Darwin Duo 80M, Quantronix), optics/prisms, and data acquisition/processing software (LaVision, DaVis 8.2). Cameras were positioned on a rigid frame not connected to the water flume. Camera 1 looked upwards at the volume of interest (VOI, horizontal slab with dimensions of approximately $60 \times 15 \times 60\,\mathrm{mm}^3$), while cameras 2 to 4 observed the VOI from above [Fig. 1(b)]. Cameras 1 and 2 were positioned in a wall-normal plane extending from the channel's side wall at in-plane angles of about 30° with the wall-normal axis. Similarly, cameras 3 and 4 were positioned in a wall-parallel plane located at the center of the VOI. Cameras 1 and 2 were equipped with 105-mm lenses (MicroNikkor) and cameras 3 and 4 with 200-mm lenses (Nikkor); in all cases the f-number was 16. To minimize image distortion due to refraction, water-filled prisms [37] were used, while focus was achieved by using Scheimpflug adapters. The laser beam was expanded and collimated using two cylindrical lenses and passed through a knife edge filter to ensure well-defined edges of

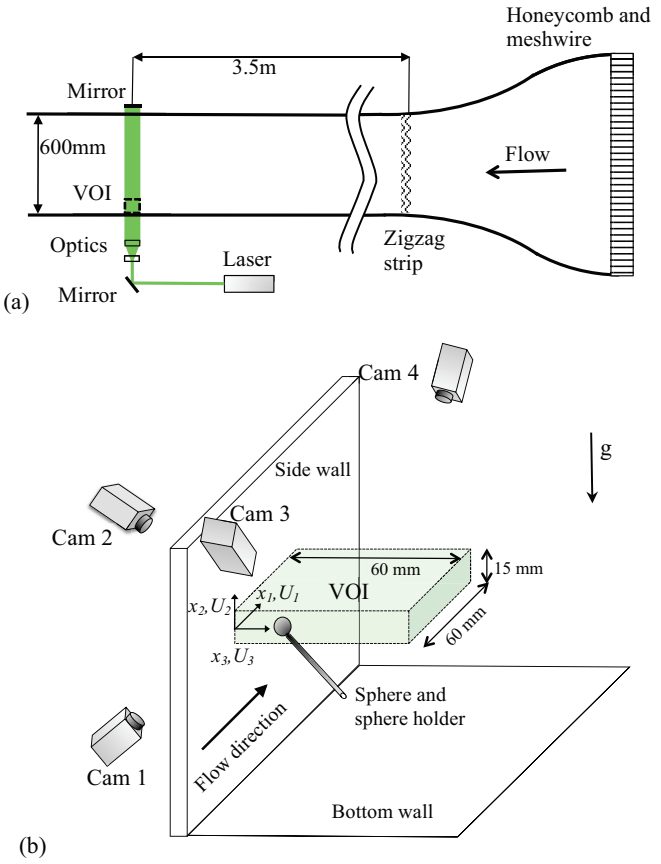

FIG. 1. Schematic layout of the experimental setup. (a) Top view of channel (not to scale); (b) employed coordinate system, camera setup, sphere position, and VOI.

the VOI in the x_2 direction (see Fig. 1). Here, x_i ($i = 1, 2, 3$) denote the streamwise, transverse, and wall-normal coordinates, respectively [Fig. 1(b)]; U_i and u_i denote the corresponding instantaneous and fluctuating velocities (Reynolds decomposed), respectively. Root mean square (rms) values of u_i are denoted by a prime. An overbar indicates temporal averaging, and angle brackets, $< .. >$, indicate spatial averaging over the x_1 and x_2 direction unless stated differently.

Uncertainties (95% confidence intervals) of $\bar{U}_i$ and the temporally averaged Reynolds stresses were estimated by a bootstrap analysis (1000 bootstrap samples with replacement [38]). Typical uncertainties in $\bar{U}_i$ were less than 1% of $\bar{U}_1$, and in the Reynolds normal and shear stresses around 5% and 10% of $\overline{u_i u_i}$ and $\overline{u_1 u_3}$, respectively.

Time resolved tomo-PIV measurements were performed 3.5 m downstream of the zigzag trip at a free stream velocity of $U_e = 0.170 \pm 0.002$ m/s. To make sure that the light intensity was sufficient and cameras benefitted from forward light scattering, a mirror was used to reflect the expanded, collimated laser beam back to the VOI [Fig. 1(a)]. Additionally, this helped to remove the shadow cast by the sphere. The VOI was located in the middle of the channel, 300 mm above the bottom wall. As flow tracers, near-neutrally buoyant hollow glass spheres (10 μm, Sphericell, Potter's Industries) were used. The imaged tracer particle density was estimated as 0.03 particles per pixel (ppp). Data sets were acquired at an acquisition frequency, $f_a = 250$ Hz, to ensure time-resolved measurements. One set was acquired without a sphere and three with the sphere positioned at different distances from the wall. Each set comprised 3140 raw PIV images resulting in 3139 instantaneous 3D vector

maps. For convenience, we will refer to the data without the sphere as the "unperturbed TBL". Before acquiring data, the field of views (FOV's) of the cameras were carefully aligned to maximize overlap, and a double-sided, dual-plane calibration target (LaVision GmbH) was aligned with the upper plane of the VOI and translated in steps of 3 mm through the depth of the VOI such that the final calibration was based on five wall-normal planes. After calibration, the data sets were acquired and prior to reconstruction, the raw data were preprocessed by (i) subtracting a sliding minimum (with a window size of 5×5 pixels), (ii) normalization by the local average smoothed over 300 pixels, (iii) applying Gaussian smoothing (3×3 pixels), and (iv) subtracting the noise level (estimated at 5 gray levels), after which intensity values were multiplied by 10 to rescale the intensity range. To improve on the initial "target" calibration, so-called "self-calibration" [39] was performed twice to reach disparities between the back projected image data below 0.3 pixels. Subsequently the 3D particle distribution in the VOI was reconstructed using the "FastMART" algorithm (provided in DaVis 8.2). Initially, particle distributions were reconstructed across a slightly larger depth than that of the VOI to obtain the average light intensity profile, $\langle \bar{I} \rangle (x_2)$, and to estimate the reconstruction noise level. Based on this profile, the edges of the VOI were taken at $x_2 = -7.0$ and 7.7 mm. The noise level was approximately 75 gray levels, and the signal-to-noise ratio within the chosen limits of the VOI ranged from 1.7 at its edges to 3.3 at its center. Three-dimensional vector fields were obtained by direct correlation of consecutively reconstructed 3D particle distributions, taking the particle displacements at the previous time step as the initial guess (time series processing). Multipass processing (in total, six passes) was applied starting with an interrogation volume size of $96 \times 96 \times 96$ voxels that was stepwise reduced to $40 \times 40 \times 40$ voxels in the last pass at 75% overlap between adjacent interrogations. The interrogation volume size in the last processing step ensured an average of about 10 particles per interrogation volume and the resulting vector spacing (10 voxels) was 0.32 mm. Binning was applied in the first few passes to speed up the processing. In between passes, outlier removal/insertion based on a median filter and a $3 \times 3 \times 3$ Gaussian smoothing filter was applied [36]. Note that when the sphere was present, its wake characteristics were processed using a smaller initial interrogation volume, i.e., $54 \times 54 \times 54$ voxels, to resolve the large velocity gradients in this region and to resolve the recirculating wake.

In the unperturbed TBL, the mean streamwise velocity, $\langle \bar{U}_1 \rangle$, can be well fitted by a canonical turbulent boundary layer profile (see Fig. 4) and is properly resolved in the buffer layer and log layer. $\langle \bar{U}_2 \rangle$ and $\langle \bar{U}_3 \rangle$ displayed magnitudes of less than 5% and 1% of $\langle \bar{U}_1 \rangle$, respectively, over most of the x_3 range most likely due to weak secondary flows or small misalignment. The boundary layer thickness based on the x_3 position where $\langle \bar{U}_1 \rangle = 0.99 U_e$, was $\delta = 45.0 \pm 1.0$ mm corresponding to a Reynolds number, $\mathrm{Re}_\delta = U_e \delta / \nu = 7050 \pm 217$. The displacement thickness was calculated as $\delta^* = 6.73 \pm 0.03$ mm, the momentum thickness as $\theta = 4.79 \pm 0.02$ mm, resulting in a shape factor, $\delta^*/\theta = 1.41$, i.e., representative of a zero-pressure gradient TBL [40,41]. The friction velocity, $u_\tau = 0.0085 \pm 0.0001$ m/s, was determined by the Clauser chart method [42], assuming $\kappa = 0.41$ for the Von Kármán constant, and for the intercept, $B = 5.0$. Reynolds numbers based on the momentum thickness and friction velocity are $\mathrm{Re}_\theta = \theta U_e / \nu = 752 \pm 9$ and $\mathrm{Re}_\tau = u_\tau \delta / \nu = 352 \pm 11$, respectively. This Re_θ has been covered by both DNS ([43] and references therein) and experiments [44].

The unperturbed TBL was perturbed by placing a steel sphere with a diameter, $D = 6.00 \pm 0.05$ mm ($D^+ = D u_\tau / \nu = 50.0 \pm 0.4$), held in place by a cylindrical supporting rod ($d = 1.00 \pm 0.05$ mm, $d^+ = 8.3 \pm 0.4$, see Fig. 2) at three distances $h = 5.4$, 13.7 and 37.6 ± 0.05 mm ($h^+ = 43$, 110 and 306 ± 0.4) from the wall (measured from the sphere center to the wall). The rod with a length of 2.3 cm was hold in place by a cylinder (diameter of 4.0 mm, length 4.4 cm) that was attached to a horizontally oriented, hydro-dynamically designed profile (length 25.5 cm) lowered from above into the channel flow. The sphere was spray-painted black to limit light reflections. Sphere Reynolds numbers based on the mean streamwise velocity of the unperturbed TBL, $\langle \bar{U}_1 \rangle_c$, the shear parameter, $K = (D \partial \langle \bar{U}_1 \rangle / \partial x_3) / \langle \bar{U}_1 \rangle_c$, the turbulence intensity of the incident unperturbed TBL, $I_t = u_1' / \langle \bar{U}_1 \rangle_c$, and other data pertinent to the present experiments are summarized in Table I. The subscript "c" denotes evaluation of the unperturbed TBL velocities at the sphere center position. Note that the rod

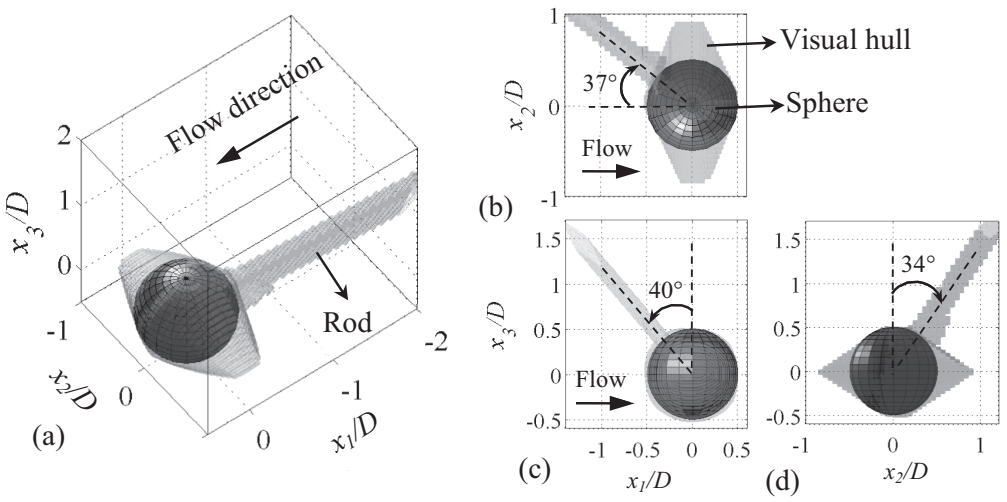

FIG. 2. Visual hull, sphere and supporting rod inside the VOI. (a) 3D surface plot and projections onto (b) x_1-x_2, (c) x_1-x_3, and (d) x_2-x_3 planes. Attachment point coordinates of rod on sphere are: $x_1/D = -0.30$, $x_2/D = 0.22$, and $x_3/D = 0.33$.

inevitably disturbs the flow but it is expected that the small-scale energy introduced into the flow through wake shedding will be much lower than that by the sphere. Therefore, we expect that the rod will have a minor effect on the sphere wake beyond the immediate vicinity of the sphere. This will be evaluated in Sec. IV where the energy spectra are discussed.

Data processing with the sphere present was different than that of the unperturbed TBL. To avoid "ghost" particles near and at the position of the sphere leading to spurious vectors, the sphere's visual hull [45] was used to mask the reconstructed particle volumes prior to calculating the 3D vector fields. First, binary masks based on projections of the sphere and holder in the four different camera views were reconstructed in the same manner as the particles in the VOI. The resulting visual hull together with the sphere is depicted in Fig. 2(a) at the same resolution as the reconstructed vector maps (10 voxels in depth). The resemblance of the visual hull to the actual object depends on the number of cameras and their spatial arrangement. Here, projections of the visual hull in different planes shown in Figs. 2(b) to 2(d) indicate that it resembles a double cone and only the projection in the x_1-x_3 plane is nearly circular. The visual hull was used to mask the reconstructed particle volume by multiplying each x_1-x_3 plane at different depth (x_2) positions by the corresponding plane of the visual hull (acting as a 3D mask). Vector maps (obtained in DaVis 8.2) were exported to Matlab where they were temporally and spatially filtered to suppress measurement noise, using a second-order polynomial regression [46]. First, the temporal signal was least-square fitted over 7 points in time corresponding to 28 ms, i.e., of the same order as the viscous time scale, $\nu/u_\tau^2 \sim$ 14 ms. Subsequently, a spatial filter was performed on the $7 \times 7 \times 7$ neighborhood around each point corresponding to $2.26 \times 2.26 \times 2.26\,\mathrm{mm}^3$ ($18.3 \times 18.3 \times 18.3$ wall units). Note that neither the temporal nor the spatial filter is expected to remove any relevant information on the near-wall

TABLE I. Summary of experimental conditions, $D = 6.00 \pm 0.05$ mm ($D^+ = 50.0 \pm 0.4$).

h^+	Re_D	$\langle \bar{U}_1 \rangle_c$ [m/s]	$u'_{1,c}$ [m/s]	$I_{t,c}$	$\bar{L}_{w,c}/D$	$\bar{L}_{w,a}/D$	K
43	692 ± 15	0.12	0.016	0.13	1.08	1.24	0.204
110	796 ± 18	0.14	0.011	0.078	1.34	1.45	0.063
306	959 ± 21	0.167	0.0056	0.033	1.66	1.66	0.016

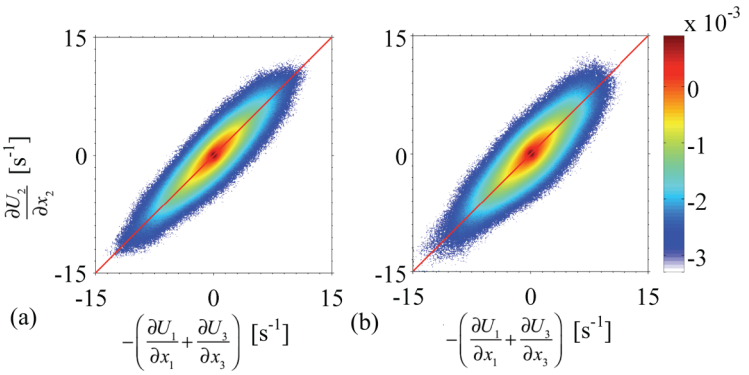

FIG. 3. Joint pdf's in the unperturbed TBL at $x_2 =$ (a) 0.0 mm, (b) 2.6 mm.

turbulent flow structures and those in the wake of the sphere where time and spatial scales are expected to be larger. The regression was also used to determine the local velocity gradients. For detailed information on the implementation of the regression, the reader is referred to Elsinga *et al.* [47]. Subsequently, components of the vorticity, $\omega_i = \partial U_i/\partial x_j - \partial U_j/\partial x_i$, were determined, and vortices were visualized using the Q-criterion [48] that identifies vortices of an incompressible flow as connected fluid regions with a positive second invariant of the velocity gradient tensor:

$$Q = \tfrac{1}{2}(\|\boldsymbol{\Omega}\|^2 - \|\boldsymbol{S}\|^2) > 0, \tag{1}$$

where $\boldsymbol{\Omega}$ and $\boldsymbol{S}$ are the antisymmetric and symmetric parts of the velocity gradient tensor, respectively. Thus, the Q-criterion detects the regions where the vorticity magnitude prevails over the strain-rate magnitude.

III. UNPERTURBED TURBULENT BOUNDARY LAYER

A. Data quality assessment

The data quality of the obtained 3D velocity fields and in particular the accuracy of the velocity gradients was assessed by checking if the continuity equation for an incompressible fluid:

$$\partial U_1/\partial x_1 + \partial U_2/\partial x_2 + \partial U_3/\partial x_3 = 0, \tag{2}$$

holds inside the VOI. Joint probability density functions (pdf's) of $\partial U_2/\partial x_2$ and $-(\partial U_1/\partial x_1 + \partial U_3/\partial x_3)$ are shown in Fig. 3 for data points sampled in two different wall normal planes located at $x_2 = 0$, and 2.6 mm. Note that if the continuity equation is perfectly satisfied, the joint pdf should collapse onto the red diagonal. As observed in Fig. 3, the joint pdf represents an elongated ellipse. The residuals of the continuity equation [Eq. (2)] are small near the center of the VOI [Fig. 1(a)], and the R^2 value was 0.7 only slightly lower than that reported by Casey *et al.* [49]. Further away from the center [Fig. 1(b)], the ratio between the major and minor axes of the joint pdf becomes less as the residuals increase near the edges of the VOI. This results in decreased accuracy of quantities based on velocity gradients such as the vorticity and the Q-criterion [Eq. (1)].

B. Mean velocity and Reynolds stress profiles

The temporally and spatially averaged streamwise velocity profile in the wall-normal direction normalized using inner scaling is depicted in Fig. 4 and compared to mean velocity profiles measured by De Graaff and Eaton [50] for $\mathrm{Re}_\theta = 1430$ and 5200. Besides being averaged over the total depth (x_2 direction) of the VOI, the present data was split in depth into three equal parts to check whether the mean velocity profile changes with x_2. As observed in Fig. 4, differences are small and in all cases profiles collapse with those of De Graaff and Eaton [50] in the buffer layer as well as in the

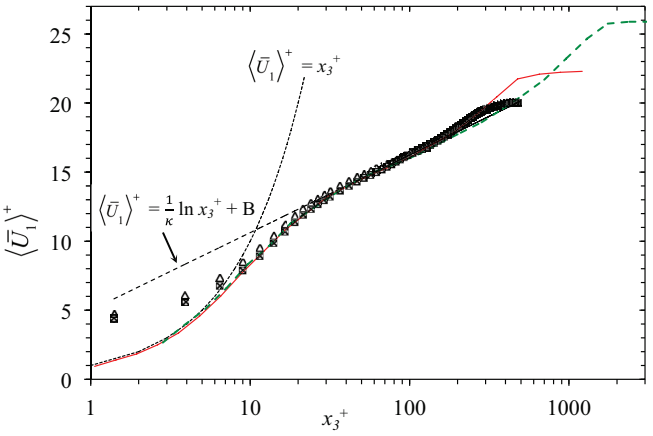

FIG. 4. Mean streamwise velocity profiles normalized by inner wall parameters in the wall-normal direction of the unperturbed TBL. Present data: $\mathrm{Re}_\theta = 752$, spatially averaged over □ total depth, △ $-7.5\,\mathrm{mm} < x_2 < -2.5\,\mathrm{mm}$, □ $-2.5\,\mathrm{mm} < x_2 < 2.5\,\mathrm{mm}$, ◯ $2.5\,\mathrm{mm} < x_2 < 7.5\,\mathrm{mm}$; DeGraaff and Eaton (2000): —— $\mathrm{Re}_\theta = 1430$, --- $\mathrm{Re}_\theta = 5200$.

log layer. In the present case, the loglike layer extents to $x_3^+ \approx 150$, less than that of the profiles by De Graaff and Eaton [50] in agreement with the present lower Re_θ. This also provides an indication of the data quality and accuracy, where only the data near to the wall (i.e., the first two points within the viscous sublayer) deviate.

Wall-normal profiles of the Reynolds normal and shear stresses plotted in inner scaling are depicted in Fig. 5, and compared to available literature data at different Re_θ by De Graaff and Eaton [50] and Erm and Joubert [44]. Similar as for $\langle \bar{U}_1 \rangle$, data was spatially averaged across different depths to assess any changes with regard to the x_2 position, in particular "edge" effects. For the normal stresses, the effect of depth position is more significant than for $\langle \bar{U}_1 \rangle$ (Fig. 4). Normal stresses near the outer edges [$-7.5\,\mathrm{mm} < x_2 < -2.5\,\mathrm{mm}$ and $2.5\,\mathrm{mm} < x_2 < 7.5\,\mathrm{mm}$ in Figs. 5(a) and 5(b)] display slightly lower maximum values than those averaged over the middle section of the VOI [$-2.5\,\mathrm{mm} < x_2 < 2.5\,\mathrm{mm}$ in Figs. 5(a) and 5(b)] and the near-wall peak of $\langle \overline{u_1 u_1} \rangle^+$ at about $x_3^+ = 25$ can only be clearly discerned in the middle section of the VOI. Note that the near-wall peak is slightly shifted away from $x_3^+ = 15$ due to limited spatial resolution. In addition, due to the contribution of noise, $\langle \overline{u_1 u_1} \rangle^+$ does not decrease to zero for $x_3^+ < 10$, and hereafter the first four points of $\langle \overline{u_1 u_1} \rangle^+$ will not be displayed. Peak values of the normalized Reynolds normal stresses [Figs. 5(a) and 5(b)] decrease with decreasing Re_θ as illustrated by comparing the present results to those of De Graaff and Eaton [50] at $\mathrm{Re}_\theta = 1430$ and 5200 and those by Erm and Joubert [44] at $\mathrm{Re}_\theta = 697$ and 1003. The present peak value of $\langle \overline{u_1 u_1} \rangle^+$ (not considering the first four points) is only slightly lower than those of Erm and Joubert [44] but is about 50% lower than those by De Graaff and Eaton [50]. Peak values of $\langle \overline{u_3 u_3} \rangle^+$ [Fig. 5(b)] are about half of those by De Graaff and Eaton [50] at much higher Re_θ.

Wall-normal profiles of the Reynolds shear stress, $-\langle \overline{u_1 u_3} \rangle^+$, depicted in Fig. 5(c) indicate the largest inhomogeneity in depth especially with regard to the obtained peak value near the wall at $x_3^+ \approx 20$ that ranges from 0.9 in the middle section to 0.7 near the edges of the VOI. The observed spatial inhomogeneity is the result of the combined effect of the reduced data quality near the edges of the VOI and partially converged data. Taking into account Re_θ effects, the general shape of the present results compares well with those obtained by De Graaff and Eaton [50] at much higher Re_θ.

IV. INSTANTANEOUS FLOW STRUCTURE

The instantaneous flow structure in the sphere wake (Fig. 6) as well as in the TBL near the wall [Figs. 6(c) to 6(f)] is illustrated by 3D isosurface plots depicting vortices (in blue) as well as the

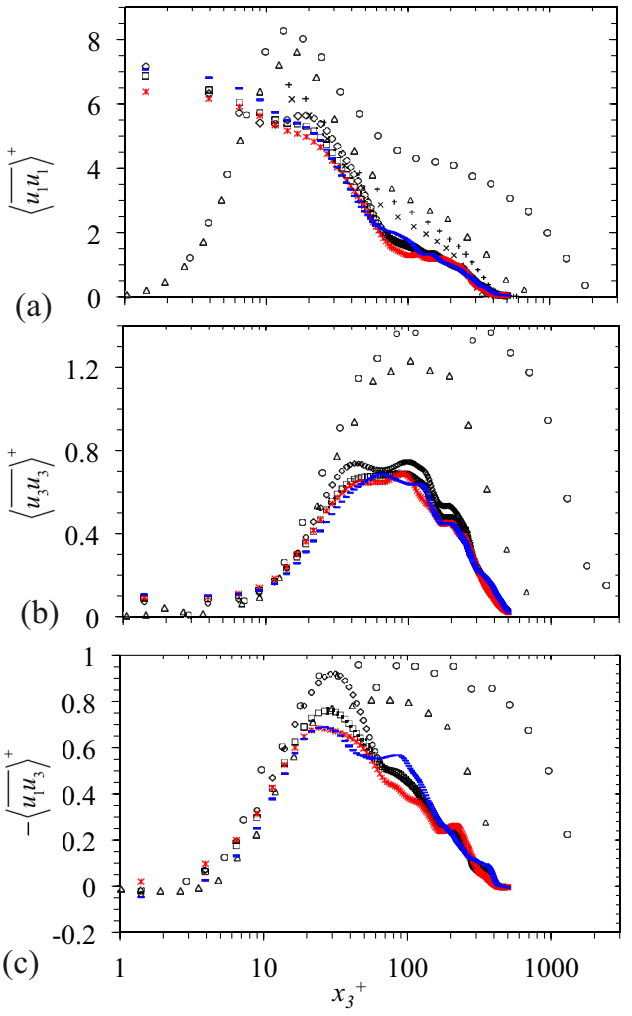

FIG. 5. Wall-normal profiles of the Reynolds normal and shear stresses normalized by inner wall parameters of the unperturbed TBL. (a) $\langle\overline{u_1u_1}\rangle^+$, (b) $\langle\overline{u_3u_3}\rangle^+$, (c) $-\langle\overline{u_1u_3}\rangle^+$. Present data: $\mathrm{Re}_\theta = 752$, spatially averaged over the streamwise direction and over the □ total depth, ✳ $-7.5\,\mathrm{mm} < x_2 < -2.5\,\mathrm{mm}$, ◇ $-2.5\,\mathrm{mm} < x_2 < 2.5\,\mathrm{mm}$, ⎯ $2.5\,\mathrm{mm} < x_2 < 7.5\,\mathrm{mm}$; DeGraaff and Eaton (2000): △ $\mathrm{Re}_\theta = 1430$, ○ $\mathrm{Re}_\theta = 5200$; Erm and Joubert (1991): × $\mathrm{Re}_\theta = 697$, + $\mathrm{Re}_\theta = 1003$.

associated instantaneous negative (red) and positive (green) velocity correlations, $(u_1u_3)^+$ (associated movies are available as supplemental electronic material [51–53]). The sphere and visual hull (Figs. 2 and 6) is shown in gray, here and in subsequent 3D plots. It can be observed that the sphere wake is densely populated by vortices, both shed from the sphere itself as well as from the supporting rod. As expected at these Re_D (see Table I), in the wake of the sphere itself, many archlike structures are observed that generate strong positive and negative u_1u_3 correlations. When the sphere is brought closer to the wall [e.g., Figs. 6(e) and 6(f)], several hairpinlike structures exhibiting a vertical plane of symmetry with their "heads" tilted away from the wall can be discerned in the near-wake of the sphere. Here, we define "arches" as relatively small curved vortices without "legs" (i.e., longitudinal vortex tubes) while "hairpins" are defined as vortices in the shape of a hairpin including longitudinal vortex "legs" [54]. The "head" of the hairpin denotes the "loop" through which the two legs connect.

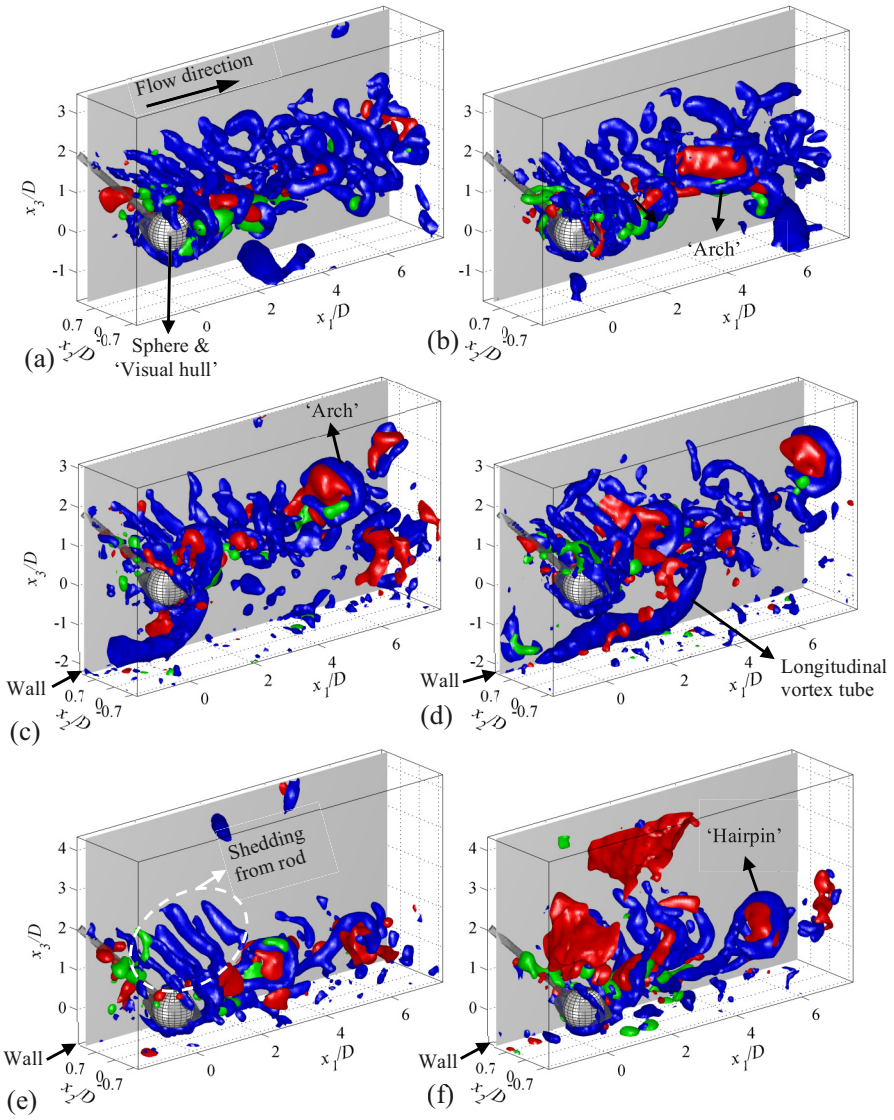

FIG. 6. Instantaneous snapshots of vortices in the wake of the sphere (blue: vortices visualized by the Q-criterion) and instantaneous velocity correlations $(u_1u_3)^+$ (red: $(u_1u_3)^+ = -6.92$ and green: $(u_1u_3)^+ = 6.92$. $h^+ = 306$: (a) $t^+ = 17.7$, (b) $t^+ = 27.7$; $h^+ = 110$: (c) $t^+ = 65.5$, (d) $t^+ = 72.9$; $h^+ = 43$: (e) $t^+ = 201.8$, (f) $t^+ = 414.9$. Spatial coordinates are referenced from the sphere center. Associated movies can be found at the Journal's website [51–53].

The hairpin vortices are shed by the sphere and are associated with negative u_1u_3 correlations. They are especially present when the sphere is positioned at $h^+ = 43$, and their orientation and alignment appear to be the result of the sphere's close vicinity to the wall. In contrast, when the sphere is positioned farther from the wall, "arches" are oriented more randomly. Interaction of the sphere with the coherent TBL structures is observed for all sphere positions, least so when the sphere is positioned at $h^+ = 306$, i.e., in the outer layer where the incident turbulence can be considered intermittent and weak compared to the wake turbulence. When positioned closer to the wall, the sphere is from time to time "engulfed" by strong near-wall structures, e.g., illustrated by the large "patches" of negative

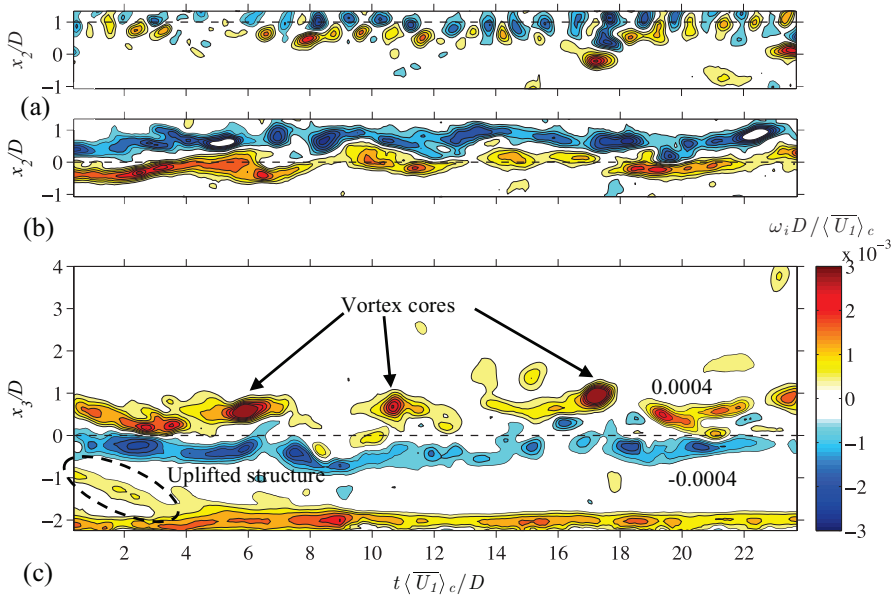

FIG. 7. Spatiotemporal plots ($h^+ = 110$) of vorticity components sampled at $x_1/D = 2.0$. (a) $\omega_3 D/\langle \bar{U}_1 \rangle_c$ at $x_3/D = 1$, (b) $\omega_3 D/\langle \bar{U}_1 \rangle_c$ at $x_3/D = 0$ and (c) $\omega_2 D/\langle \bar{U}_1 \rangle_c$ at $x_2/D = 0$. Contour level spacing is 0.0004 and two levels are given in (c). Black dashed lines indicate examples of sampling positions in Fig. 8.

$u_1 u_3$ correlations that are observed above the sphere in Fig. 6(f). With the sphere positioned at $h^+ = 110$, TBL structures are observed as longitudinal vortex tubes passing underneath the sphere [see Figs. 6(c) and 6(d)].

An example of the temporal evolution of the flow in the wake of the sphere is provided in Fig. 7 through spatiotemporal plots of the out-of-plane components of the vorticity, ω_2 and ω_3, as a function of time, t, nondimensionalized by D and $\langle \bar{U}_1 \rangle_c$ ($h^+ = 110$). Similar plots were obtained at the other h^+. The plots were constructed by sampling the vorticity components in time along lines placed at $x_1/D = 2.0$ in wall-normal and wall-parallel planes. They provide a time sequence of shear layers and vortices crossing this line. Sampling lines in wall-parallel planes were positioned at two distances from the sphere: one at the center of the sphere [$x_3/D = 0$, Fig. 7(b)], and the other at $x_3/D = 1.0$ [Fig. 7(a)] to visualize the vortex shedding in the wake of the supporting rod. At all sphere positions, shedding at $x_2/D = 2$ resembled a train of oppositely signed vortices connected by shear layers [e.g., Figs. 7(b) and 7(c)]. In the equatorial wall-normal plane, the near wall TBL is seen as a region of high positive vorticity with occasionally uplifted structures [Fig. 7(c), dash ellipse] that are the planar signatures of the uplifted elongated vortex tubes [see Figs. 6(c) and 6(d)].

To determine the vortex shedding frequencies, power spectral densities (PSDs) of the instantaneous wall normal velocity were determined by dividing the current data set into subsets of 1-s duration. For each subset, the PSD was calculated using a fast Fourier transform and applying a Hanning window [55]. Subsets were 50% overlapped in time and resulting PSD's were averaged over all subsets. "Probes" were positioned at several locations in the wake of the sphere (examples shown as black dashed lines in Fig. 7). PSDs sampled at different positions inside the wake of the sphere displayed variability both in space as well as in time, pointing at the complex interaction between the coherent structures in the TBL and shed vortices from the sphere and the rod. Averaged PSDs sampled at $x_1/D = 2.0$ and 4.0 are displayed in Fig. 8 for all three sphere positions. In all cases, distinct frequency peaks (values reduced with increasing x_1/D) were obtained just downstream of both the supporting rod and the sphere. The peaks broadened and maximum values were reduced when the sphere was positioned closer to the wall, which can be attributed to dissipation as well as the interaction

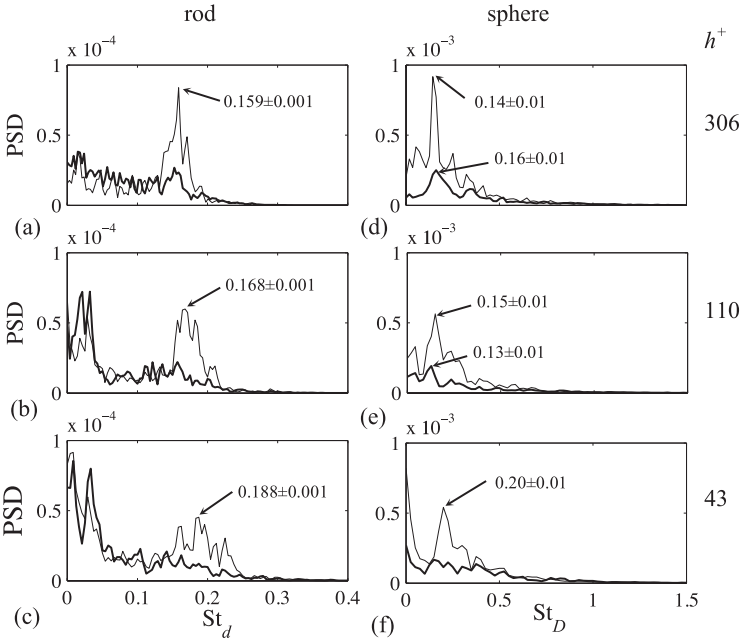

FIG. 8. Averaged power spectral densities of U_3 sampled at different points with respect to the sphere. Left column sampled in the wake of the rod at $x_2/D = x_3/D = 1.0$. Right column sampled in the wake of the sphere at (d), (e) $x_2/D = x_3/D = 0$, and (f) at $x_2/D = 0.5$, $x_3/D = 0$. Thin solid curves sampled at $x_1/D = 2.0$ and thick solid curves sampled at $x_1/D = 4.0$. Example sampling positions are shown in Fig. 7 as dashed lines. Note that there is an order of magnitude difference in the spectral amplitude between the graphs on the left and those on the right.

between the TBL structures and the shed vortices. Strouhal numbers corresponding to sphere vortex shedding at $x_1/D = 2.0$ were $\mathrm{St}_D = f_s D/\langle \bar{U}_1 \rangle_c = 0.14$, 0.15 and 0.20 at $h^+ = 306$, 110 and 43, and $\mathrm{Re}_D = 959$, 796 and 692, respectively. For a sphere in uniform flow [13], the Strouhal number ranges are: 0.18–0.21 ($\mathrm{Re}_D = 700$), 0.19–0.20 ($\mathrm{Re}_D = 800$), 0.19–0.21 ($\mathrm{Re}_D = 960$, low-frequency mode), and 0.25–0.31 ($\mathrm{Re}_D = 960$, high frequency mode). Therefore, except when the sphere was positioned at $h^+ = 43$, the present St_D are lower than those obtained in the wake of a sphere in a uniform flow. Note that there are no published experimental results on vortex shedding frequencies of small spheres immersed in a turbulent boundary layer. However, compared to spheres in uniform flow, uniform shear increased St_D [56], while upstream turbulence ($I_t \approx 0.04$) slightly lowered St_D in the experiments by Wu and Faeth [20] and strongly decreased St_D in the DNS by Zeng *et al.* [6]. Note that the latter were estimated based on the time history of the lift force acting on the sphere. In our measurements, the turbulence intensity was similar or larger than 0.04 [6,20] (Table I), while the shear parameter was in the range reported by Sakamoto and Haniu [56]. Effects of Reynolds number, turbulence intensity, wall proximity, and changing shear parameter may all be important in the present results.

Unfortunately, the sphere could not be fixed without the support rod and its effect on sphere shedding was twofold. First, the attachment point caused some azimuthal asymmetry and second, shed vortices from the rod might affect and interact with those shed by the sphere. The latter can be evaluated based on the data presented in Figs. 6 to 8. Figure 6(e) ($h^+ = 43$, dash ellipse) shows a coherent staggered pattern of inclined elongated vortices shed immediately downstream of the support rod, further illustrated in the spatiotemporal plots of $\omega_3 D/\langle \bar{U}_1 \rangle_c$ ($h^+ = 110$) sampled at $x_1/D = 2.0$ and $x_3/D = 1.0$ depicted in Fig. 7(a). Clearly, ordered sequences of vortices are shed at a much higher frequency than in the wake of the sphere in agreement with rod Reynolds numbers

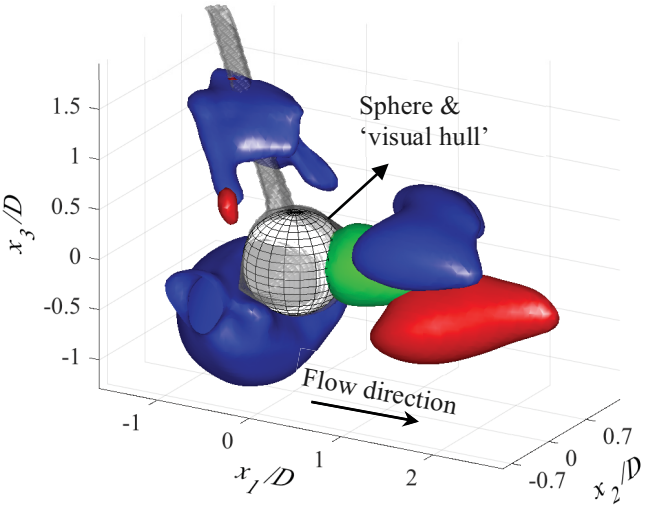

FIG. 9. 3D isosurface plot of the edge of the mean recirculating wake (Green: $\bar{U}_1/U_e = 0$) and $\bar{U}_3/U_e$ in the vicinity of the sphere ($h^+ = 110$). Blue: $\bar{U}_3/U_e = -0.059$; Red: $\bar{U}_3/U_e = 0.088$.

(based on d) that range from 115 to 160, i.e., well beyond the onset of vortex shedding. However, the question remains how much these shed vortices affect the shedding in the wake of the sphere. Looking at the PSDs presented in Fig. 8, it is clear that there is at least an order of magnitude difference between the energy contained in the wake of the rod and the sphere. Furthermore, no distinct frequency peak associated with rod shedding is observed at the sphere wake's centerline [Figs. 8(d) to 8(f)] nor in the wake of the rod at $x_1/D = 4.0$ [thick solid curves in Figs. 8(a) to 8(c)]. Therefore, based on these results, we conclude that any effects of rod shedding on the sphere wake are negligible beyond $x_1/D = 4.0$. However, in the near wake ($x_1/D < 4.0$), rod attachment leads to some azimuthal asymmetry in mean velocities and turbulence statistics as will be shown in the next section.

V. MEAN WAKE FLOW CHARACTERISTICS

A. Mean velocities

A representative illustration of the mean 3D flow pattern around the sphere is presented in Fig. 9 ($h^+ = 110$) by 3D isosurface plots representing the edge of the mean recirculating wake in green ($\bar{U}_1/U_e = 0$) and positive and negative $\bar{U}_3$ isosurfaces in red and blue, respectively. The mean recirculating wake resembles a half prolate spheroid extending from the rear of the sphere with lobes of positive and negative $\bar{U}_3$ extending from its periphery. Positive $\bar{U}_3$ isosurfaces have a well-defined conelike shape, unlike the negative $\bar{U}_3$ isosurface downstream of the sphere that resembles a hornlike structure as a result of the flow disturbance by the supporting rod that also limits the upward directed flow just upstream of the sphere.

Contour plots of $\bar{U}_1/U_e$ in equatorial wall-normal and wall-parallel planes are depicted in Fig. 10 for all three sphere positions. Here and in subsequent contour plots, the sphere is depicted by a filled circle in wall-normal planes and by the cross-section of the visual hull [Fig. 2(b)] in wall-parallel planes; its center position is depicted by a "+" symbol. In all cases, just downstream of the sphere, a mean recirculating wake ($\bar{U}_1 < 0$, in blue) is observed. Upon approaching the wall, it is increasingly tilted away from it. Its length can either be defined as the distance between the rear of the sphere and the downstream position along the sphere's centerline where $\bar{U}_1$ changes sign, $\bar{L}_{w,c}$ [Fig. 10(b)], or as the actual recirculating wake length, $\bar{L}_{w,a}$, measured as the maximum distance between the rear of the

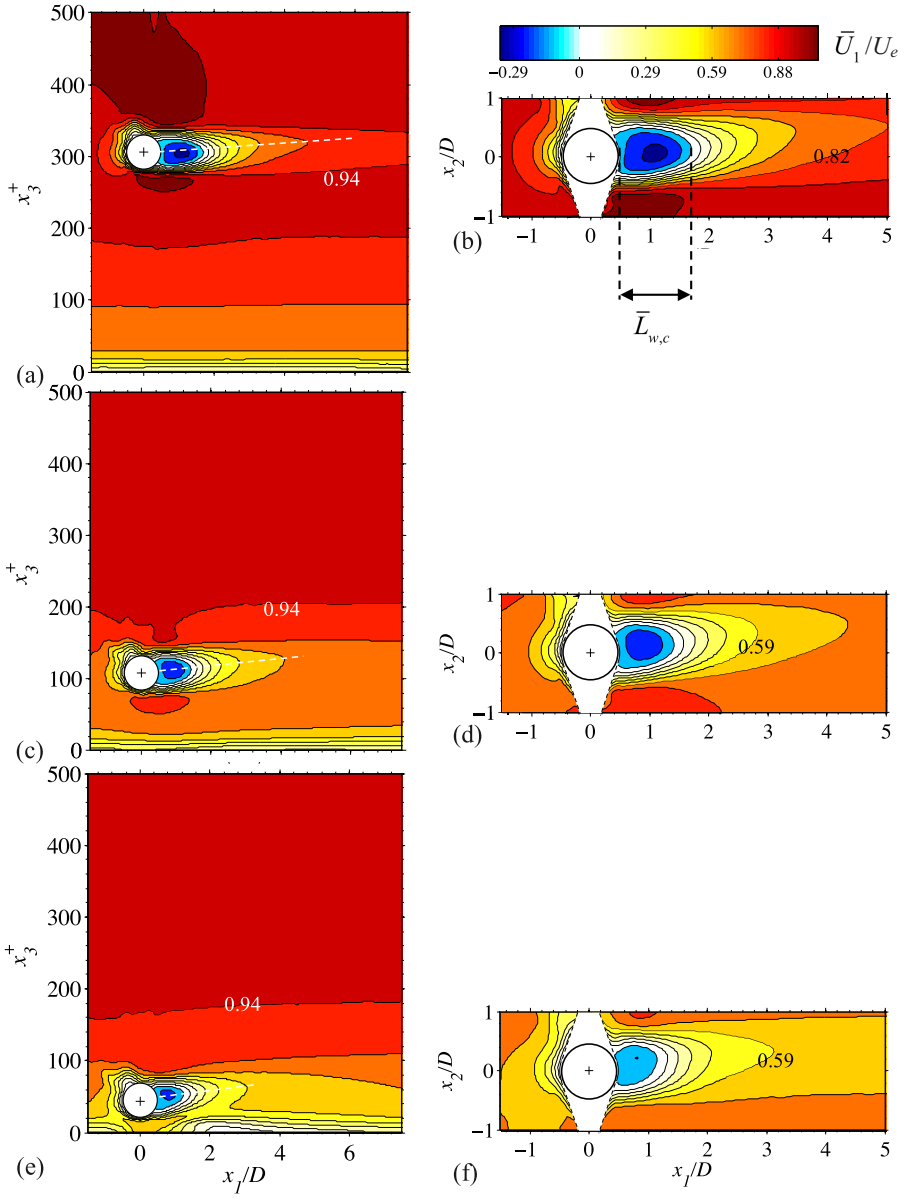

FIG. 10. Contour plots of the temporally averaged, normalized streamwise velocity in wall-normal (left column) and wall-parallel equatorial planes (right column). h^+ is (a), (b) 306, (c), (d) 110, (e), (f) 43. Contour spacing is 2/17; in each counterplot one level is given.

sphere and the downstream position where $\bar{U}_1/U_e = 0$ ($\bar{L}_{w,a} \geqslant \bar{L}_{w,c}$, Table I). The ratio $\bar{L}_{w,c}/\bar{L}_{w,a}$ equals unity at $h^+ = 306$ and is reduced to 0.92 and 0.87 at $h^+ = 110$ and 43, respectively, while $\bar{L}_{w,a}$ is reduced from $1.66D$ to $1.08D$ when the sphere is positioned at $h^+ = 306$ and 43, respectively. Note that $\bar{L}_{w,a}$ at $h^+ = 306$ exceeds that reported by Zeng *et al.* [6], i.e., $\bar{L}_{w,a} \approx 1.29D$ (DNS), for a sphere positioned at the center of a turbulent channel flow at similar turbulence intensity but significantly lower Re_D (= 455). Contour plots indicate that the near wake tilt angle [its orientation indicated by a white dashed line in Figs. 10(a), 10(c), and 10(e)] is 3.9° at $h^+ = 306$ and increases to

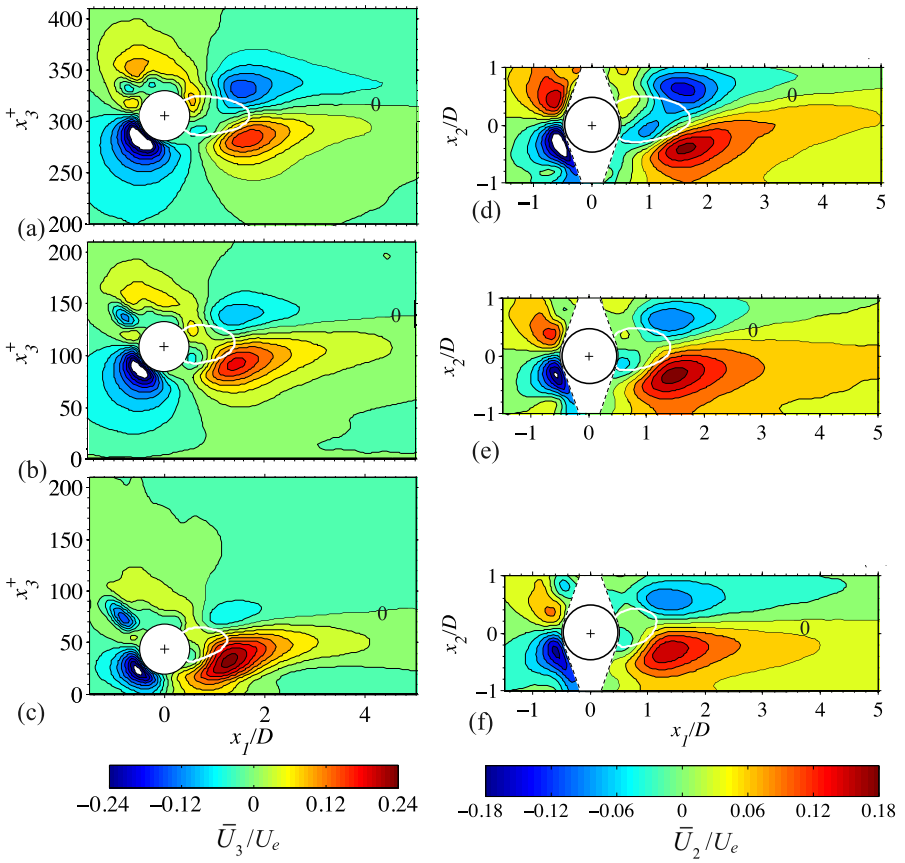

FIG. 11. Contour plots of the temporally averaged, normalized wall-normal (left column) and transverse (right column) velocity in equatorial planes. $h^+ =$ (a), (d) 306; (b), (e) 110; (c), (f) 43. Contour spacing is 1/34; in each counterplot one level is given. Solid white curve denotes the edge of the mean recirculating wake.

5.7° and 9.1° when the sphere is positioned at $h^+ = 110$ and 43, respectively, similar as reported in the DNS by Zeng *et al.* [6] at lower Re_D. Note that the deflection of the near wake away from the wall contrasts with that observed for spheres immersed in a laminar boundary layer flow for which the wake is tilted towards the wall as a result of self-induced motion of the double-threaded, longitudinal wake structure [31,57]. In the present case, the flow in the wake of the sphere is highly unsteady and characterized by archlike structures (Fig. 6) unlike the steady double-threaded, longitudinal wake structure observed in laminar flow. This, in combination with inviscid effects due to flow acceleration around the sphere, results in deflection of the wake away from the wall [6] as will be further discussed in Sec. VI. Contour plots of $\bar{U}_1$ in wall-parallel planes [Figs. 10(b), 10(d), and 10(f)] show that the wake is also slightly tilted (5° to 7°) toward the positive x_2 direction. This angle is independent of the sphere position relative to the wall and is most likely the result of the asymmetry caused by the supporting rod.

Similar contour plots, but now of $\bar{U}_2/U_e$ and $\bar{U}_3/U_e$, are depicted in Fig. 11 in the vicinity of the sphere. Note that $|\bar{U}_3|$ [Figs. 11(a) to 11(c)] is an order of magnitude larger than the weak secondary flow ($<0.01\langle\bar{U}_1\rangle$) in the unperturbed TBL (Sec. II). The edge of the mean recirculating wake ($\bar{U}_1/U_e = 0$, Fig. 10) is plotted in Fig. 11 (and in subsequent figures when relevant) as either a white or black curve. When the sphere is positioned at $h^+ = 306$ [Figs. 11(a) and 11(d)], contours of $\bar{U}_3$ depict the familiar pattern of nearly antisymmetric, diagonally placed "blobs" of negative and

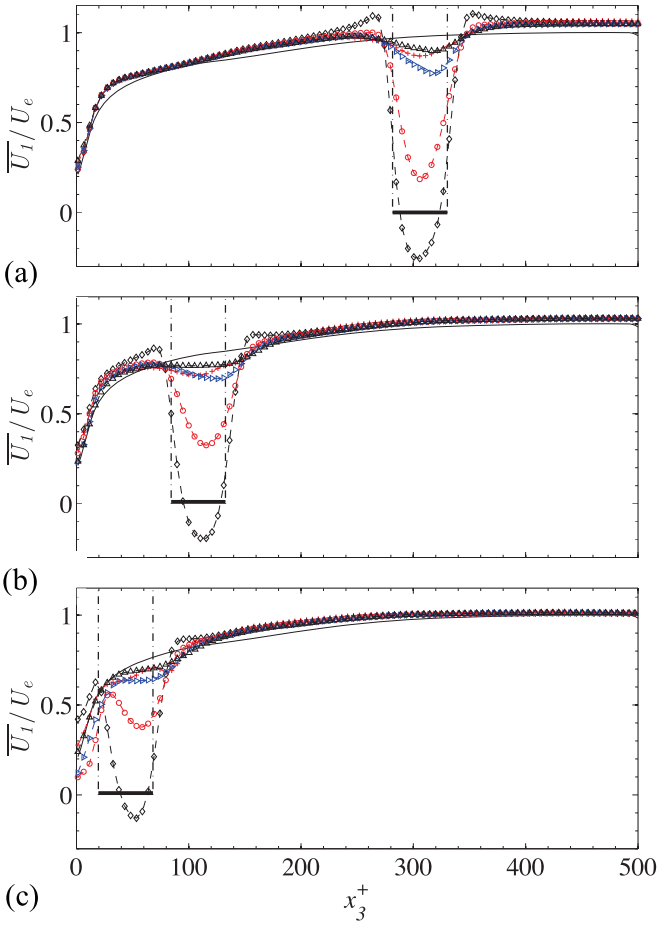

FIG. 12. Profiles of the normalized, mean streamwise velocity sampled at different x_1/D in the wall-normal, equatorial plane ($x_2/D = 0$). —— Unperturbed TBL; h^+ = (a) 306, (b) 110, (c) 43; $x_1/D = -1$ (+), 1 (◇), 2 (○), 4 (▷), 7 (△). Horizontal black bars denote the sphere position and dash-dot lines its edges.

positive mean velocity as the flow is diverted past the sphere, similar as obtained in the wake of a sphere held stationary in a uniform flow [58]. Note that slightly upstream and on top of the sphere (here "top" meaning away from the wall), the supporting rod fragments the upward directed flow [e.g., Fig. 11(a)]. In the wake of the sphere, $|\bar{U}_3|/U_e$ and $|\bar{U}_2|/U_e$ peak at the edge of the recirculating wake where vortex shedding occurs. Upon approaching the wall [Figs. 11(b) and 11(c)], antisymmetry is increasingly lost as the downward and upward directed fluid at the bottom of the sphere (here "bottom" meaning closest to the wall) strengthen, while the upward and downward moving fluid on top of the sphere weaken. Closest to the wall [Fig. 11(c)], the flow emerges from the gap between the wall and the sphere similar to a tilted wall jet. The present results qualitatively resemble the measurements by Ozgoren *et al.* [27] who investigated the effect of reducing gap size on the near wake flow of a large sphere ($D \sim \delta$) positioned in a turbulent boundary layer at much higher Re_D ($2{,}500 < \mathrm{Re}_D < 10{,}000$).

Profiles of $\bar{U}_1/U_e$ sampled at several x_1/D ($x_2/D = 0$) are compared to the unperturbed TBL in Fig. 12. Just in front of the sphere at $x_1/D = -1$, $\bar{U}_1$ decreases as the flow is displaced which leads to velocities in excess of those in the undisturbed TBL in the vicinity of the sphere, extending several diameters away from it [6]. At the VOI's edge ($x_3{}^+ = 500$) and for all h^+ and x_1/D, velocities nearly

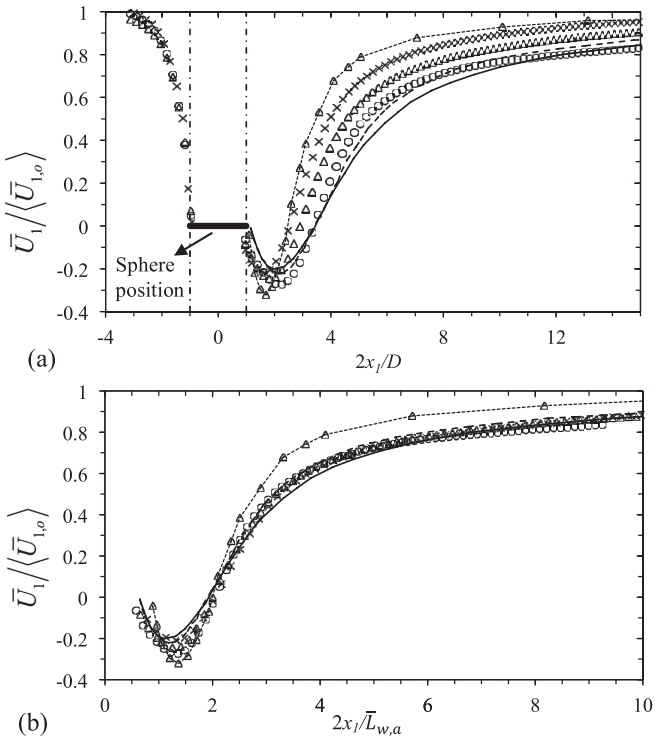

FIG. 13. The normalized mean streamwise velocity in the wake of the sphere sampled along the position where $\bar{U}_1$ is minimum. Data plotted versus (a) $2x_1/D$ and (b) $2x_1/\bar{L}_{w,a}$. $h^+ =$ ○ 306, △ 110, × 43; present data is plotted at twice the vector spacing; -△-- Amoura *et al.* (2010), $\mathrm{Re}_D = 1080$; Zeng *et al.* (2010): ——— $\mathrm{Re}_D = 325$, ---- $\mathrm{Re}_D = 455$.

collapse and differences with the unperturbed TBL are reduced from 4% to 0% when positioning the sphere closer to the wall. Close to the wall, $\bar{U}_1$ is affected by the sphere and profiles at $x_1/D = 7$ indicate that the flow does not fully recover to the undisturbed TBL. Note that recovery occurs fastest when the sphere is positioned closest to the wall and for $h^+ = 43$ and $x_1/D = 7$ the perturbed and unperturbed profiles collapse up to $x_3^+ \approx 40$ [Fig. 12(c)]. The peak velocity deficit is increasingly shifted away from the wall in agreement with the increasing tilt of the wake with decreasing h^+.

The recovery of the velocity deficit in the wake of the sphere was examined by sampling the local minimum, streamwise velocity which provides a realistic estimate of the recovery in case the wake is not axisymmetric. It is plotted in Fig. 13(a) as a function of $2x_1/D$ and normalized by the corresponding, local mean streamwise velocity of the unperturbed TBL, $\langle \bar{U}_{1,o} \rangle$, where the subscript "$o$" denotes "unperturbed TBL." Also included are the velocities upstream of the sphere sampled along the axis extending from the sphere's center. The present results are compared to experiments by Amoura *et al.* [23] and DNS by Zeng *et al.* [6] both lacking any wall effects. Upstream of the sphere within a distance of $1.5D$, $\bar{U}_1/\langle \bar{U}_{1,o} \rangle$ quickly drops to zero. Minimal $\bar{U}_1/\langle \bar{U}_{1,o} \rangle$ decrease from -0.2 at $h^+ = 43$ to -0.4 at $h^+ = 306$ and $\bar{L}_{w,a}$ decreases when moving closer to the wall (Table I). Beyond $\bar{L}_{w,a}$, values increase at a decreasing rate and $\bar{U}_1/\langle \bar{U}_{1,o} \rangle$ recovers fastest when the sphere is positioned at $h^+ = 43$. Note that when $\bar{U}_1$ was sampled along the sphere axis in the streamwise direction, $\bar{U}_1/\langle \bar{U}_{1,o} \rangle$ approached unity at $2x_1/D = 14$ for all sphere positions (not shown).

Neither our data sets nor those of Amoura *et al.* [23] and Zeng *et al.* [6], collapse when plotted versus $2x_1/D$. Since it can be assumed that the recirculating wake length incorporates effects of the ambient turbulence, the wall as well as the vortex shedding, the results depicted in Fig. 13(a) were

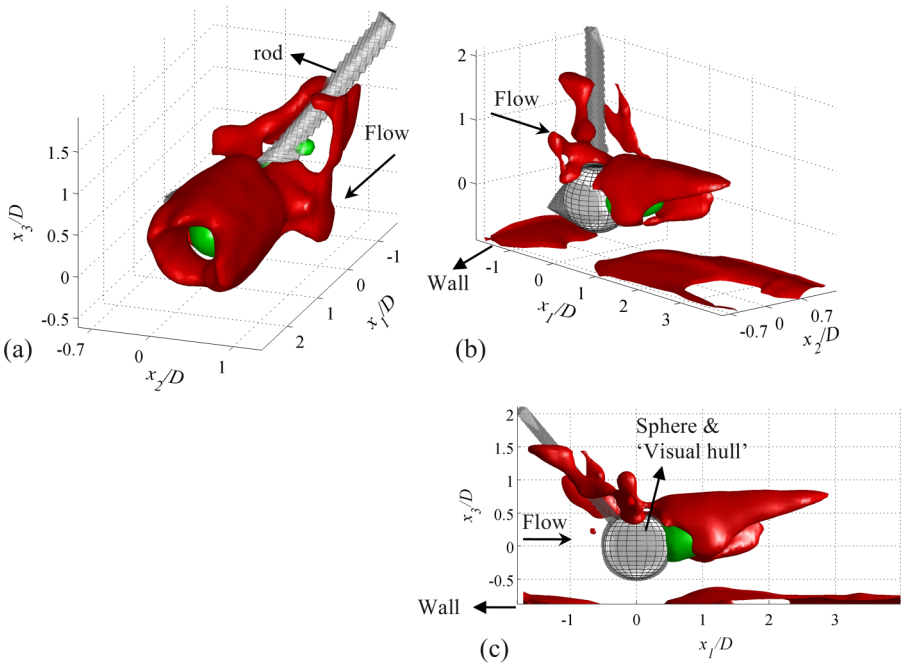

FIG. 14. Iso-surface plots depicting the mean recirculating wake (green: $\bar{U}_1/U_e = 0$) and $\overline{u_1u_1}^+$ (= 11.1 in red). h^+ = (a) 110 and (b, c) 43.

replotted in Fig. 13(b) versus $2x_1/\bar{L}_{w,a}$. Somewhat surprisingly, the present results for different h^+ collapse well beyond $\bar{L}_{w,a}$ despite the fact that the spheres are exposed to different flow regions resulting in different Reynolds numbers, turbulence intensities and shear parameters (Table I). Interestingly, the present data sets do not collapse with those of Amoura *et al.* [23] but do so with

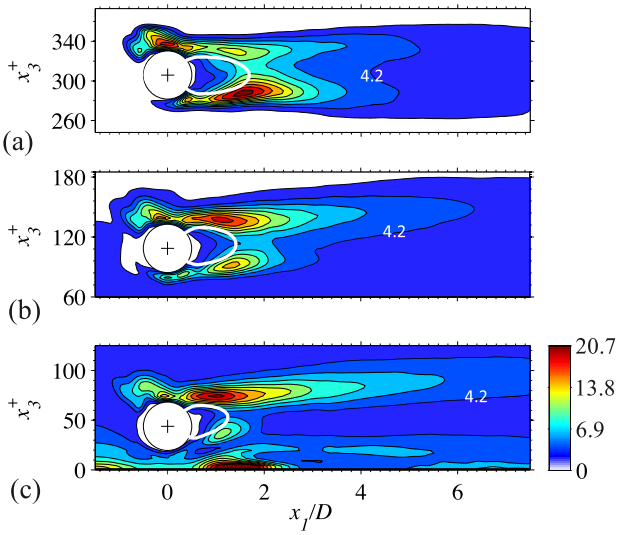

FIG. 15. Contour plots of $\overline{u_1u_1}^+$ in wall-normal equatorial planes. h^+ = (a) 306, (b) 110, (c) 43. Contour level spacing 2.1; one contour level is given. Solid white curve denotes the edge of the mean recirculating wake.

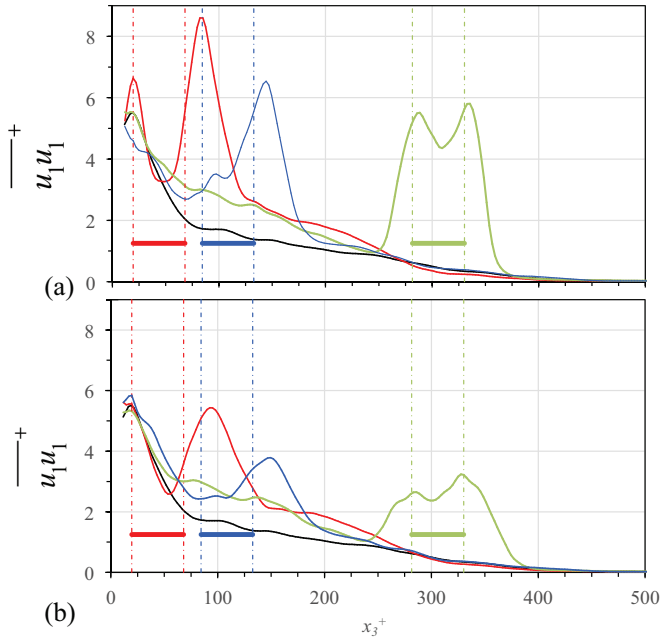

FIG. 16. Profiles of $\overline{u_1u_1}^+$ taken at $x_2/D = 0$ and $x_1/D =$ (a) 4, (b) 7. Curves: unperturbed TBL (black), sphere positioned at $h^+ = 43$ (red), 110 (blue), 306 (green). Horizontal bars denote the sphere position and dash-dot lines its edges.

those of Zeng *et al.* [6] whose Re_D (= 325 and 455) were lower than ours, but still high enough for vortex shedding to occur. Note that other data sets provided by Zeng *et al.* [6] at lower Re_D (no vortex shedding) did not collapse. Furthermore, the results reported by Zeng *et al.* [6] lack any wall effects but $I_t = 0.04$, similar as our results at $h^+ = 306$. In the case of Amoura *et al.* [23], $\mathrm{Re}_D = 1080$, i.e., similar to the present Re_D when the sphere is positioned at $h^+ = 306$. However, their incident

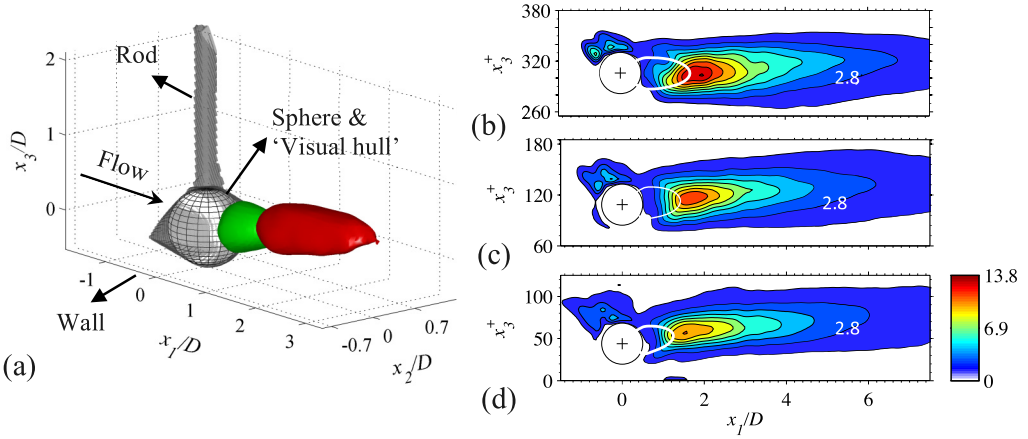

FIG. 17. Distribution of $\overline{u_3u_3}^+$ in the wake of the sphere. (a) 3D isosurface plot of the mean recirculating wake (green $\bar{U}_1/U_e = 0$) and $\overline{u_3u_3}^+$ (= 6.9 in red), $h^+ = 43$. Contour plots of $\overline{u_3u_3}^+$ in the wall-normal equatorial plane. $h^+ =$ (b) 306, (c) 110, (d) 43. Contour level spacing 1.4; one contour level is given. Solid white curve denotes the edge of the mean recirculating wake.

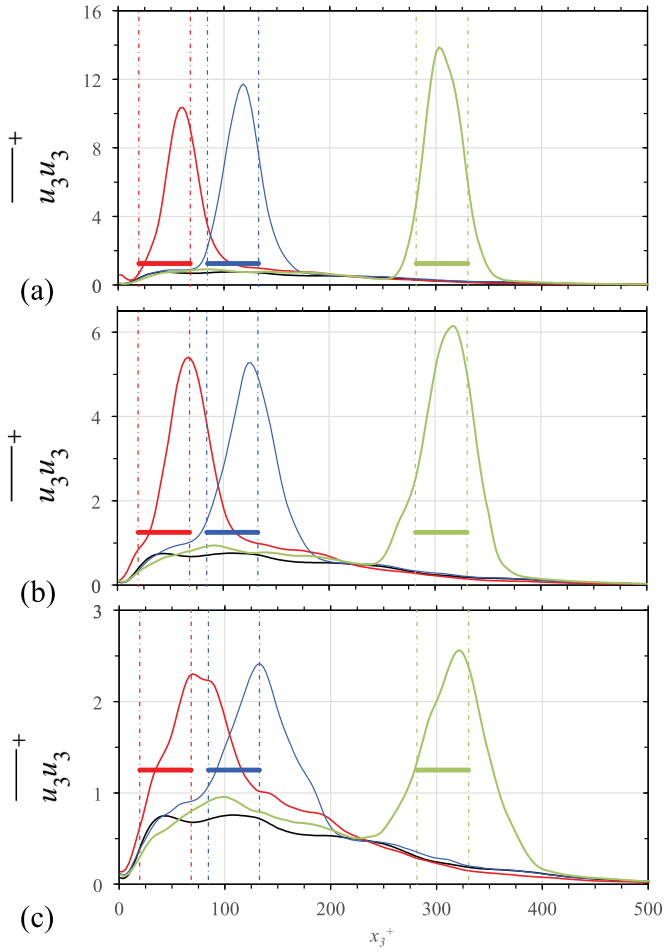

FIG. 18. Profiles of $\overline{u_3u_3}^+$ at $x_2/D = 0$ and $x_1/D =$ (a) 2, (b) 4, (c) 7. Curves: unperturbed TBL (black), sphere positioned at $h^+ = 43$ (red), 110 (blue), 306 (green). Horizontal bars denote the sphere position and dash-dot lines its edges.

turbulence had an integral length scale comparable to D and $I_t = 0.26$, i.e., much higher than in the present case (Table I). They showed that in their case recovery of the velocity deficit in the near wake (beyond $\bar{L}_w$) was governed solely by ambient incident turbulence. In our case, wall effects, ambient turbulence, and vortex shedding cannot be disentangled and all may affect $\bar{L}_{w,a}$. However, based on the above-presented comparison to results of Amoura *et al.* [23] and Zeng *et al.* [6], wall proximity seems to have a negligible effect. More data across a wider parameter range is needed to further corroborate these results.

B. Reynolds stresses

The distribution of the streamwise component of the normalized Reynolds stress, $\overline{u_1u_1}^+$, in the wake of the sphere positioned at $h^+ = 110$ and 43, is illustrated by 3D isosurface plots in Fig. 14. The isosurface depicted in Fig. 14(a) ($h^+ = 110$) shows that $\overline{u_1u_1}^+$ is distributed as a more or less cylindrical, tapered shell extending from the edge of the mean recirculating wake. Approaching the wall leads to asymmetry in the distribution of $\overline{u_1u_1}^+$ with reduced values below the sphere [Figs. 14(b) and 14(c)], further illustrated in the contour plots of $\overline{u_1u_1}^+$ in equatorial wall-normal planes shown

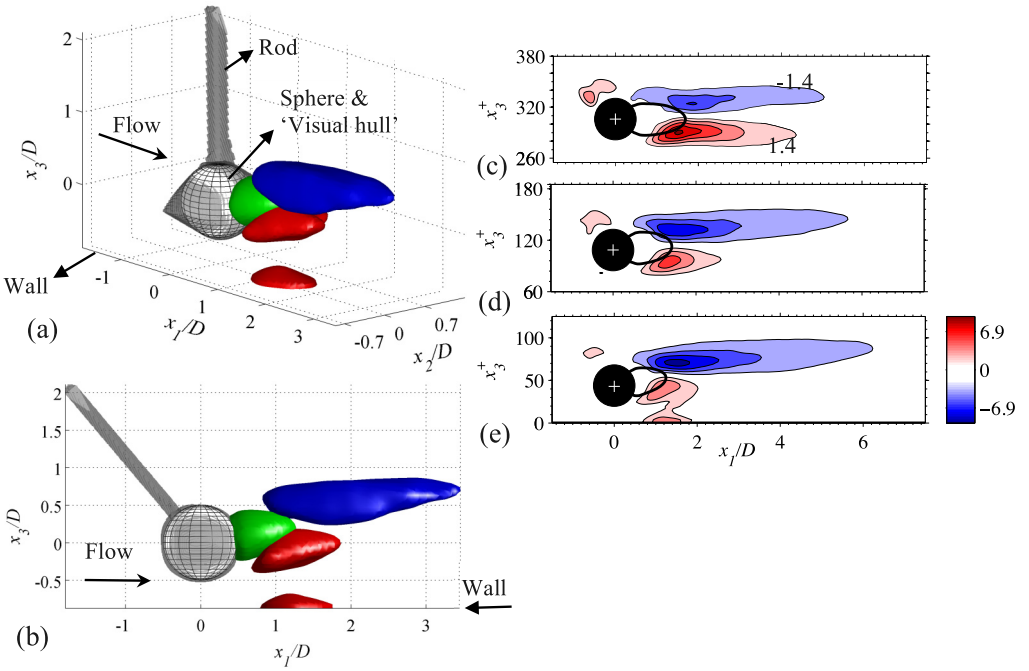

FIG. 19. Distribution of $\overline{u_1u_3}^+$ in the wake of the sphere. (a) 3D isosurface plot of the mean recirculating wake (green $\bar{U}_1/U_e = 0$) and $\overline{u_1u_3}^+$ in the wake of the sphere ($h^+ = 43$). Red: $\overline{u_1u_3}^+ = 2.8$, blue: $\overline{u_1u_3}^+ = -4.2$, (b) side view. Contour plots of $\overline{u_1u_3}^+$ in equatorial planes. $h^+ =$ (c) 306, (d) 110, and (e) 43. Contour level spacing is 1.4; two levels are given in (c). Solid black curve denotes the edge of the mean recirculating wake.

in Fig. 15. Wall effects are strongest when the sphere is positioned at $h^+ = 43$ [Figs. 14(b), 14(c), and 15(c)], and instead of a tubular shell, the $\overline{u_1u_1}^+$ isosurface [Figs. 14(b) and 14(c)] extends solely from the upper side of the mean recirculating wake as a slightly upward directed, tapered part of a cone. Near the wall just downstream of the sphere, elevated values of $\overline{u_1u_1}^+$ are observed. Note that the effect of the supporting rod (see also Sec. IV) on the distribution of $\overline{u_1u_1}^+$ was most felt when the sphere was positioned at $h^+ = 306$. It caused an azimuthal asymmetry appearing as an "indent" in the $\overline{u_1u_1}^+$ isosurface (not shown) and decreased values in the contour plot depicted in Fig. 15(a) ($x_3^+ \approx 330$, $0.5 \leqslant x_1/D \leqslant 2.0$). Probably due to the interaction with the TBL, the disturbance of the supporting rod was reduced when the sphere was located at $h^+ = 110$ and the cylindrical shell wrapped around the mean recirculating wake was smooth without any noticeable indent [Fig. 14(a)].

Profiles of $\overline{u_1u_1}^+(x_3^+)$ with the sphere present and extracted at $x_1/D = 4$ and 7 ($x_2/D = 0$) are compared in Fig. 16 to the unperturbed TBL. Obtained peak values increased when the sphere was positioned closer to the wall, and in all cases profiles had similar shapes at $x_1/D = 4$ and 7 albeit with reduced values at the latter position. When the sphere was positioned at $h^+ = 306$ [$x_1/D = 4$, Fig. 16(a)], the familiar, nearly symmetrical "double hump" pattern was obtained indicating that the wall effect was small at this position. The symmetrical "double hump" pattern was lost when the sphere was positioned at $h^+ = 110$, while at $h^+ = 43$ it seemed to exist solely as a result of the near-wall peak observed for the unperturbed TBL. The effect of the wall is to tilt the wake away from it, and as a result the peak value of $\overline{u_1u_1}^+$ was pushed further outwards and increasingly away from the edge of the sphere with increasing x_1/D (Fig. 16). Recovery to the unperturbed TBL did not occur within the VOI, but the canonical near wall peak was recovered at $x_1/D = 4$ for $h^+ = 306$, while at $x_1/D = 7$ it was approached for all h^+. Interestingly, when the sphere was located at $h^+ = 306$, values of $\overline{u_1u_1}^+$ were elevated between $50 < x_3^+ < 250$.

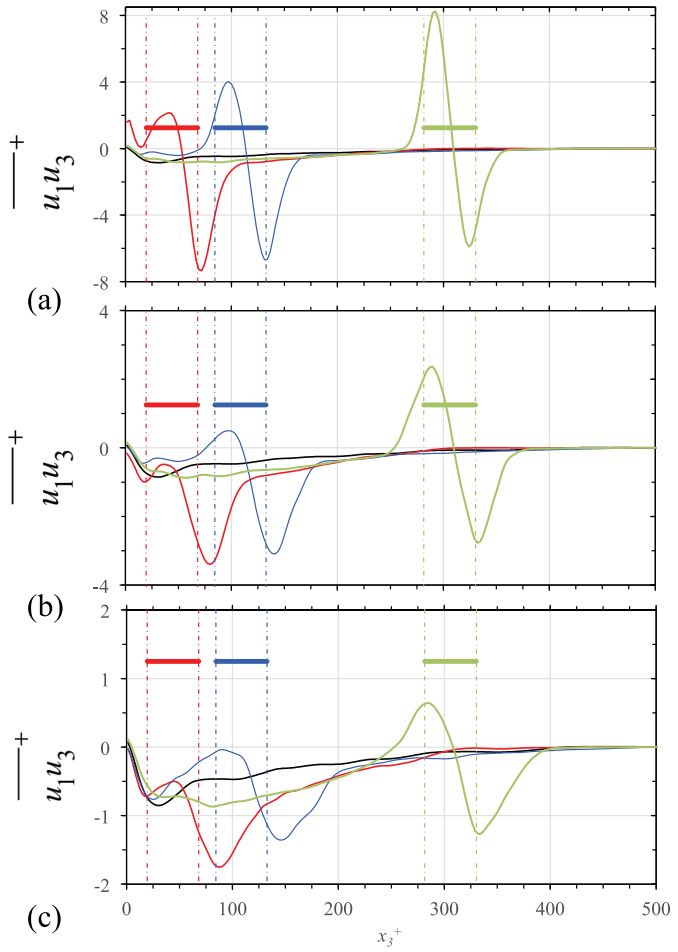

FIG. 20. Wall-normal profiles of $\overline{u_1u_3}^+$ at $x_2/D = 0$ and $x_1/D =$ (a) 2, (b) 4, (c) 7. Curves: unperturbed TBL (black), sphere positioned at $h^+ = 43$ (red), 110 (blue), 306 (green). Horizontal bars denote the sphere position and dash-dot lines its edges.

In contrast to $\overline{u_1u_1}^+$, the 3D distribution of $\overline{u_3u_3}^+$ depicted in Fig. 17(a) ($h^+ = 43$) resembles a cone (red) extending downstream from the sphere off the tip of the mean recirculating wake (green). Similar distributions were obtained when the sphere was positioned at $h^+ = 306$ and 110 as well as for $\overline{u_2u_2}^+$ (not shown). Wall-normal equatorial cross-sections [Figs. 17(b) to 17(d)] indicate that maximum values of $\overline{u_3u_3}^+$ occur off the tip of the mean recirculating wake, decreasing upon approaching the wall. Profiles of $\overline{u_3u_3}^+(x_3^+)$ sampled at $x_1/D = 2, 4$, and 7 ($x_2/D = 0$) are compared to the undisturbed TBL in Fig. 18. Profiles display a single maximum, its value decreasing with increasing x_1/D. For a given sphere position, peak positions move away from the wall with increasing x_1/D. Like $\overline{u_1u_1}^+$ (Fig. 16), the unperturbed TBL is not recovered within the VOI.

The normalized Reynolds shear stress component, $\overline{u_1u_3}^+$, presented in Figs. 19(a) and 19(b) for $h^+ = 43$ as 3D iso-surface plots, shows that the Reynolds shear stress is distributed as tapered negative (in red) and positive (in blue) "lobes" extending from the edge of the mean recirculating wake. The effect of the wall reduces the magnitude of the positive $\overline{u_1u_3}^+$ lobe and increases that of the negative $\overline{u_1u_3}^+$ lobe as can be observed in the contour plots of $\overline{u_1u_3}^+$ in equatorial planes presented in Figs. 19(c) to 19(e). These results qualitatively correspond to those reported by Ozgoren

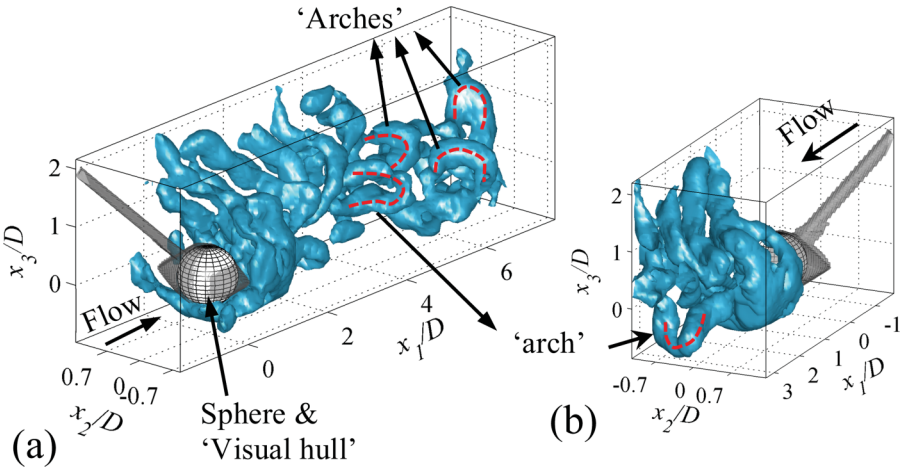

FIG. 21. Typical snapshot of vortices visualized by the Q-criterion in the wake of the sphere positioned at $h^+ = 306$. (a) and (b) are different 3D projections. Red dashed lines indicate curvature of arches.

et al. ([27], $D \sim \delta$) who also found that the magnitude of the Reynolds shear stress closest to the wall in the wake of the sphere is strongly diminished upon reducing the gap size.

Comparing the wall-normal profiles of $\overline{u_1 u_3}^+$ sampled at $x_1/D = 2$, 4 and 7 ($x_2/D = 0$) to the undisturbed TBL (Fig. 20) reveals that similar as the normal stresses, the undisturbed TBL is not recovered. However, the near-wall ($x_3{}^+ < 20$) undisturbed TBL is approached at $x_1/D = 7$, while substantial differences exist in the range $50 < x_3{}^+ < 200$. Magnitudes of $\overline{u_1 u_3}^+$ decrease with increasing x_1/D and when the sphere is positioned at $h^+ = 306$ an almost antisymmetric

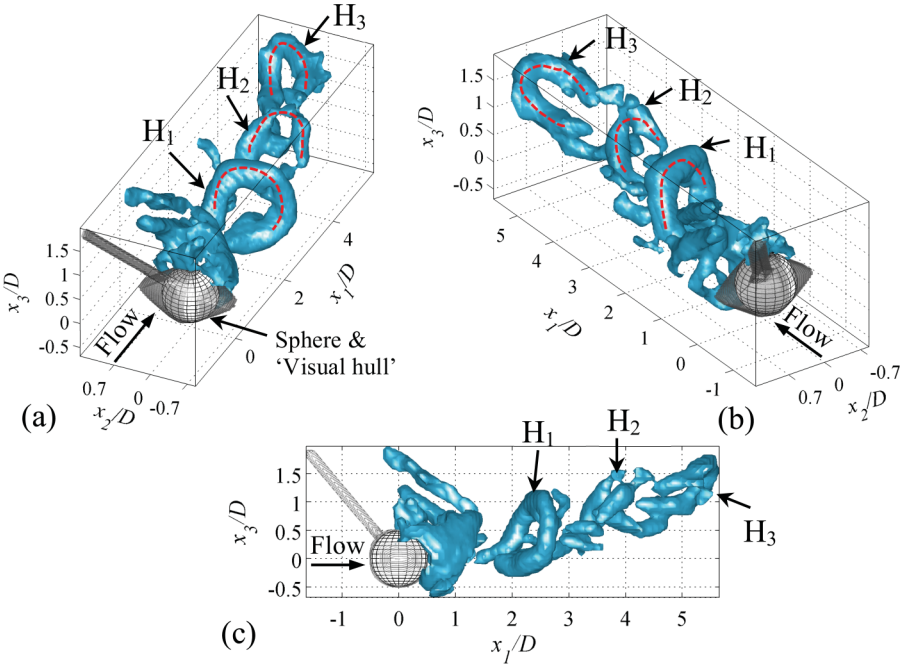

FIG. 22. Snapshot of vortices visualized by the Q-criterion in the wake of the sphere positioned at $h^+ = 110$. (a, b) two different 3D views and (c) projection in x_1-x_3 plane. Red dashed lines indicate curvature of arches.

"double hump" pattern is obtained with peak magnitudes located in the shear layer extending from the sphere close to its edges (dash-dot lines). As the sphere is moved closer to the wall, positive $\overline{u_1u_3}^+$ peaks decrease strongest and vanish with increasing x_1/D. The decrease of positive $\overline{u_1u_3}^+$ upon approaching the wall can be linked to the preferred orientation of the shed vortices as will be discussed next.

VI. EFFECT OF WALL PROXIMITY ON VORTEX SHEDDING

In the previous two sections, the mean flow and Reynolds stress distributions as well as the instantaneous turbulence structure of the wake of a sphere held stationary within a fully developed TBL have been discussed in depth. The main finding was that the wake of the sphere is deflected off the wall when the gap size between the wall and the sphere is decreased and axisymmetry is lost. While this has been observed previously [6,27], only a qualitative explanation has been suggested (see Sec. I). The orientation of the sphere wake is dictated by both viscous and inviscid effects. The latter are associated with flow acceleration due to displacement of the fluid around the sphere while the former are related to the vortical structure that develops in its wake as Re_D exceeds the critical Reynolds number for the onset of vortex shedding. Here, we postulate that the increasing asymmetry imposed by the wall with decreasing gap, forces the shed vortices (resembling "arches" and "hairpins") to orient themselves such that they attain an almost wall-normal-oriented symmetry plane, in contrast to shedding without wall effects where vortices lack any preferred orientation. As a result of self-induced motion, the wake is then deflected away from the wall, which implies that the lift force acting on the sphere is directed toward the wall (negative lift).

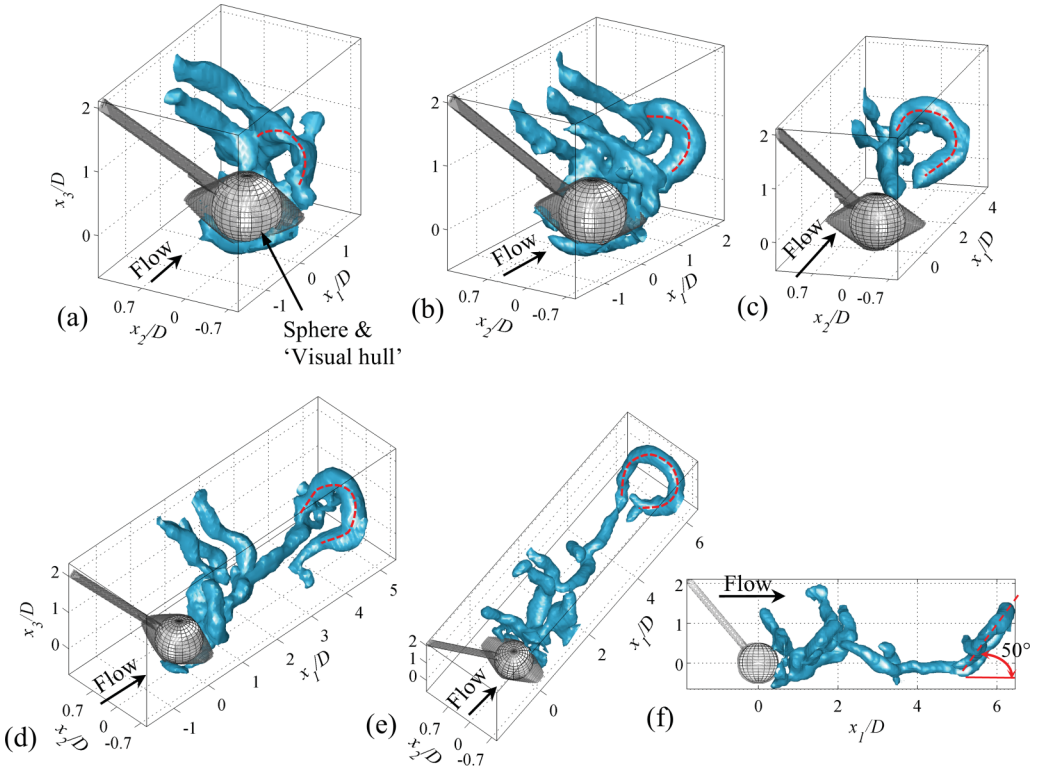

FIG. 23. Evolution of hairpin vortex in the wake of the sphere positioned at $h^+ = 43$. Time difference between snapshots (a) to (e) is $\Delta t^+ = 11.4$; (f) Projection of (e) in x_1-x_3 plane. Red dashed lines indicate curvature of arches.

To substantiate this, examples of the instantaneous vortical structure in the wake of the sphere are depicted in Figs. 21–23 for all three sphere positions. For clarity, only the largest connected structures are depicted. The sphere wake at $h^+ = 306$ ($\mathrm{Re}_D = 959$, Fig. 21) is characterized by small scale "arches" that are oriented in different directions (indicated by the dashed red curves), upwards, downwards, and to the sides. In contrast, closer to the wall ($h^+ = 110$, $\mathrm{Re}_D = 796$), the "arches" are in the majority of cases oriented parallel to the wall and in Fig. 22 an example is presented showing a train of interconnected hairpin like structures having nearly wall-normal symmetry planes (H_1 to H_3, dashed red curves). The "heads" rotate clockwise [in Fig. 22(a)] and expel fluid away from the wall and as a result of self-induction the wake is tilted upwards [Fig. 22(c)]. When the sphere is positioned at $h^+ = 43$ ($\mathrm{Re}_D = 692$), in several cases hairpinlike vortices are generated with their "heads" lifted up from the wall. An example of the evolution of such a hairpin vortex is depicted in Fig. 23, where its head at all stages is indicated by a red dashed curve. Downstream of the sphere [Figs. 23(c) and 23(d)], the hairpin's "head" and "legs" become clearly visible while the disturbance by the supporting rod becomes insignificant as previously discussed in Sec. IV. A "fully" developed hairpin vortex is observed in Figs. 23(e) and 23(f). The side view [Fig. 23(f)] clearly shows that the "legs" are oriented parallel to the wall while the head is inclined at 50° from the wall. Such well-defined hairpin vortices have been visualized for spheres in uniform flows at lower Re_D [13,16] and their appearance in the present flow configuration is facilitated by the proximity of the sphere to the wall. Also in this case, the hairpin expels fluid away from the wall resulting in upward tilting of the mean wake [Fig. 10(e)]. Note that close to the sphere, the elongated vortex tubes shed by the supporting rod interact with the toroidal vortex in the near wake of the sphere and an interconnected structure is initially shed [Figs. 23(a) and 23(b)].

VII. CONCLUSIONS

In this study, the flow in the wake of a stationary sphere immersed in a near zero-pressure gradient TBL ($\mathrm{Re}_\theta = 752$, $\mathrm{Re}_\tau = 352$) was investigated. The sphere ($D^+ = 50$) was positioned: (i) in the outer layer, (ii) start of the log layer, and (iii) the buffer layer; its center was positioned at $h^+ = 306$, 110, and 43, respectively, measured from the wall. To both temporally and spatially resolve the flow dynamics, time-resolved tomo-PIV was employed. The VOI included the sphere and had a depth of about $2D$ and a downstream distance measured from the sphere center up to about $7D$. Note that the present study extended to much higher sphere Reynolds numbers ($692 < \mathrm{Re}_D < 959$) than the DNS by Ref. [6], and vortex shedding was always present. The unperturbed TBL characteristics were first validated against existing literature results, showing that the present measurements were well resolved beyond ${x_3}^+ = 10$.

While previous measurements of the wake of a sphere positioned in a TBL were performed using low-speed planar PIV [27], here the evolving instantaneous 3D structure of shed vortices and associated Reynolds shear stress generating events was resolved. At the present range of Re_D, the wake of the sphere was densely populated by archlike structures clearly emanating from the sphere and responsible for generating Reynolds shear stress. When the sphere was positioned closest to the wall, hairpinlike coherent structures developed in the wake of the sphere with their "heads" tilted away from the wall as they were advected downstream. Furthermore, closer to the wall, the sphere's interaction with the near-wall TBL coherent structures became more intense as the latter engulfed the sphere.

The sphere wake's time averaged recirculating flow region decreased in length upon approaching the wall and tilted away from it, which resulted in asymmetric wake distributions of mean velocities and Reynolds stresses. The increased tilt close to the wall was associated with the mentioned development of hairpinlike vortices in the wake whose self-induced motion was directed away from the wall. Mean streamwise velocity recovery in the sphere wake collapsed when plotted as a function of $x_1/\bar{L}_{w,a}$. The actual mean recirculating wake length, $\bar{L}_{w,a}$, is likely affected by ambient turbulence, wall proximity as well as vortex shedding that cannot be disentangled in the present measurements.

However, a comparison with few published literature results suggested that wall proximity is of minor importance within the limited range of experimental conditions.

Spatiotemporal sequences of vorticity components showed that vortex shedding was characterized by a train of counter-rotating vortices connected by high shear regions. Their shedding frequencies showed up as prominent peaks in the PSD's of U_3 in the wake of the sphere at $x_1/D = 2.0$. Associated Strouhal numbers were lower than for a sphere in a uniform flow except when positioned at $h^+ = 43$.

With negligible wall effects, the Reynolds stress distribution of $\overline{u_1u_1}^+$ extended from the edge of the mean recirculating wake as a tubular, tapered, axisymmetric "shell", while distributions of $\overline{u_2u_2}^+$ and $\overline{u_3u_3}^+$ extended as axisymmetric domes from the downstream tip of the mean recirculating wake. Wall proximity led to preferential orientation of the shed vortices, and as a result, normal Reynolds stress distributions lost their axisymmetry and values close to the wall were attenuated. The 3D distribution of the Reynolds shear stress, $\overline{u_1u_3}^+$, was characterized by double lobes of positive and negative values distributed almost symmetrically at the top and bottom of the wake when wall effects were minimal. Wall proximity increased $\overline{u_1u_3}^+$ leading to an asymmetric distribution.

In conclusion, the present measurements have shown that tilting of the sphere wake away from the wall (implying a negative lift force) is the result of self-induced motion of shed hairpin-like vortices that attain nearly wall-normal symmetry planes whose "heads" become preferentially aligned with the wall as the sphere is positioned closer to the wall. Note that direct measurements of the forces acting on particles immersed in a turbulent boundary are extremely difficult due to their small magnitudes [28–30]. In the future, the estimation of forces acting on the body solely based on the measured flow field [59] will be pursued.

ACKNOWLEDGMENTS

This research was carried out during the first author's sabbatical leave at the TU-Delft, 3ME Aero- and Hydrodynamics Laboratory, Delft, The Netherlands. He gratefully acknowledges the enthusiastic support of all people associated with the laboratory and, in particular, Ing. E. Overmars for his help in setting up the experiments. This research was partially supported by the J.M. Burgerscentrum Research School for Fluid Mechanics and the Israel Science Foundation under Grant No. 1596/14.

[1] G. Hetsroni, Particles-turbulence interaction, Int. J. Multiph. Flow **15**, 735 (1989).
[2] M. Rashidi, G. Hetsroni, and S. Banerjee, Particle-turbulence interaction in a boundary layer, Int. J. Multiph. Flow **16**, 935 (1990).
[3] G. C. Truesdell and S. Elgobashi, On the two-way interaction between homogenous turbulence and dispersed solid particles. II particle dispersion, Phys. Fluids **6**, 1405 (1993).
[4] D. Kaftori, G. Hetsroni, and S. Banerjee, Particle behavior in the turbulent boundary layer. I. motion, deposition, and entrainment, Phys. Fluids **7**, 1095 (1995).
[5] D. Kaftori, G. Hetsroni, and S. Banerjee, Particle behavior in the turbulent boundary layer. II. velocity and distribution profiles, Phys. Fluids **7**, 1107 (1995).
[6] L. Zeng, S. Balachandar, and F. M. Najjar, Wake response of a stationary finite-sized particle in a turbulent channel flow, Int. J. Multiph. Flow **36**, 406 (2010).
[7] T. Tanaka and J. K. Eaton, Sub-kolmogorov resolution partical image velocimetry measurements of particle-laden forced turbulence, J. Fluid Mech. **643**, 177 (2010).
[8] C. Poelma and G. Ooms, Particle-turbulence interaction in a homogeneous, isotropic turbulent suspension, Appl. Mech. Rev. **59**, 78 (2006).
[9] P. Bagchi and S. Balachandar, Response of the wake of an isolated particle to an isotropic turbulent flow, J. Fluid Mech. **518**, 95 (2004).
[10] C. Wieselsberger, Der Luftwiderstand von Kugeln, Zeitschrift für Flugtechnik und Motor-Luftschiffahrt **5**, 140 (1914).
[11] W. Möller, Experimentelle Untersuchungen zur Hydrodynamik der Kugel, Phys. Zeitschrift **2**, 57 (1938).

[12] E. Achenbach, The effects of surface roughness and tunnel blockage on the flow past spheres, J. Fluid Mech. **65**, 113 (1974).
[13] H. Sakamoto and H. Haniu, A study on vortex shedding from spheres in a uniform flow, J. Fluids Eng. **112**, 386 (1990).
[14] J.-S. Wu and G. M. Faeth, Sphere wakes in still surroundings at intermediate reynolds numbers, AIAA J. **31**, 1448 (1993).
[15] T. A. Johnson and V. C. Patel, Flow past a sphere up to a reynolds number of 300, J. Fluid Mech. **378**, 19 (1999).
[16] T. Leweke, M. Provansal, D. Ormieres, and R. Lebescond, Vortex dynamics in the wake of a sphere, Phys. Fluids **11**, S12 (1999).
[17] C. Brücker, Spatio-temporal reconstruction of vortex dynamics in axisymmetric wakes, J. Fluids Struct. **15**, 543 (2001).
[18] M. Chrust, S. Goujon-Durand, and J. E. Wesfreid, Loss of a fixed plane of symmetry in the wake of a sphere, J. Fluids Struct. **41**, 51 (2013).
[19] H. J. Kim and P. A. Durbin, Observations of the frequencies in a sphere wake and of drag increase by acoustic excitation, Phys. Fluids **31**, 3260 (1988).
[20] J.-S. Wu and G. M. Faeth, Sphere wakes at moderate reynolds numbers in a turbulent environment, AIAA J. **32**, 535 (1994).
[21] J. S. Wu and G. M. Faeth, Effect of ambient turbulence intensity on sphere wakes at intermediate reynolds numbers, AIAA J. **33**, 171 (1995).
[22] D. Legendre, A. Merle, and J. Magnaudet, Wake of a spherical bubble or a solid sphere set fixed in a turbulent environment, Phys. Fluids **18**, 048102 (2006).
[23] Z. Amoura, V. Roig, F. Risso, and A. M. Billet, Attenuation of the wake of a sphere in an intense incident turbulence with large length scales, Phys. Fluids **22**, 055105 (2010).
[24] P. Bagchi and S. Balachandar, Effect of turbulence on the drag and lift of a particle, Phys. Fluids **15**, 3496 (2003).
[25] L. Zeng, S. Balachandar, P. Fischer, and F. Najjar, Interactions of a stationary finite-sized particle with wall turbulence, J. Fluid Mech. **594**, 271 (2008).
[26] T. Tsutsui, Flow around a sphere in a plane turbulent boundary layer, J. Wind Eng. Ind. Aerodyn. **96**, 779 (2008).
[27] M. Ozgoren, A. Okbaz, S. Dogan, B. Sahin, and H. Akilli, Investigation of flow characteristics around a sphere placed in a boundary layer over a flat plate, Exp. Therm. Fluid Sci. **44**, 62 (2013).
[28] D. Hall, Measurements of the mean force on a particle near a boundary in turbulent flow, J. Fluid Mech. **187**, 451 (1988).
[29] M. A. Mollinger and F. T. M. Nieuwstadt, Measurement of the lift force on a particle fixed to the wall in the viscous sublayer of a fully developed turbulent boundary layer, J. Fluid Mech. **316**, 285 (1996).
[30] C. Muthanna, F. T. M. Nieuwstadt, and J. C. R. Hunt, Measurement of the aerodynamic forces on a small particle attached to a wall, Exp. Fluids **39**, 455 (2005).
[31] L. Zeng, F. Najjar, S. Balachandar, and P. Fischer, Forces on a finite-sized particle located close to a wall in a linear shear flow, Phys. Fluids **21**, 033302 (2009).
[32] S. Lee and J. M. Wilczak, The Effects of shear flow on the unsteady wakes behind a sphere at moderate Reynolds numbers, Fluid Dyn. Res. **27**, 1 (2000).
[33] D. H. Doh, T. G. Hwang, and T. Saga, 3D-PTV measurements of the wake of a sphere, Meas. Sci. Technol. **15**, 1059 (2004).
[34] G. E. Elsinga and J. Westerweel, Tomographic-PIV measurement of the flow around a zigzag boundary layer trip, Exp. Fluids **52**, 865 (2012).
[35] G. E. Elsinga, F. Scarano, B. Wieneke, and B. W. Van Oudheusden, Tomographic particle image velocimetry, Exp. Fluids **41**, 933 (2006).
[36] R. J. Adrian and J. Westerweel, *Particle Image Velocimetry* (Cambridge University Press, Cambridge, 2011).
[37] A. K. Prasad, Stereoscopic particle image velocimetry, Exp. Fluids **29**, 103 (2000).
[38] B. Efron and R. J. Tibshirani, *An Introduction to the Bootstrap* (Chapman and Hall/CRC, London, 1993).

[39] B. Wieneke, Volume self-calibration for 3D particle image velocimetry, Exp. Fluids **45**, 549 (2008).
[40] H. Schlichting, *Boundary-Layer Theory* (McGraw-Hill, New-York, 1979).
[41] P. Schlatter and R. Örlü, Turbulent boundary layers at moderate reynolds numbers: Inflow length and tripping effects, J. Fluid Mech. **710**, 5 (2012).
[42] F. H. Clauser, The turbulent boundary layer, Adv. Appl. Mech. **4**, 1 (1956).
[43] P. Schlatter and R. Örlü, Assessment of direct numerical simulation data of turbulent boundary layers, J. Fluid Mech. **659**, 116 (2010).
[44] L. P. Erm and P. N. Joubert, Low-reynolds-number turbulent boundary layers, J. Fluid Mech. **230**, 1 (1991).
[45] D. Adhikari and E. K. Longmire, Visual hull method for tomographic PIV measurement of flow around moving objects, Exp. Fluids **53**, 943 (2012).
[46] A. Savitzky and M. J. E. Golay, Smoothing and differentiation of data by simplified least squares procedures, Anal. Chem. **36**, 1627 (1964).
[47] G. E. Elsinga, R. J. Adrian, B. W. van Oudheusden, and F. Scarano, Three-dimensional vortex organization in a high-reynolds-number supersonic turbulent boundary layer, J. Fluid Mech. **644**, 35 (2010).
[48] J. C. R. Hunt, A. A. Wray, and P. Moin, Eddies, streams, and convergence zones in turbulent flows, In Proc. 1988 Summer Program of the Center for Turbulence Research, 193, NASA Ames/Stanford University (1988).
[49] T. A. Casey, J. Sakakibara, and S. T. Thoroddsen, Scanning tomographic particle image velocimetry applied to a turbulent jet, Phys. Fluids **25**, 025102 (2013).
[50] D. B. De Graaff and J. K. Eaton, Reynolds-number scaling of the flat-plate turbulent boundary layer, J. Fluid Mech. **422**, 319 (2000).
[51] See Supplemental Material at http://link.aps.org/supplemental/10.1103/PhysRevFluids.3.024601 for instantaneous vortices in the wake of the sphere ($h^+ = 43$).
[52] See Supplemental Material at http://link.aps.org/supplemental/10.1103/PhysRevFluids.3.024601 for instantaneous vortices in the wake of the sphere ($h^+ = 110$).
[53] See Supplemental Material at http://link.aps.org/supplemental/10.1103/PhysRevFluids.3.024601 for instantaneous vortices in the wake of the sphere ($h^+ = 306$).
[54] J. Zhou, R. J. Adrian, S. Balachandar, and T. M. Kendall, Mechanisms for generating coherent packets of hairpin vortices in channel flow, J. Fluid Mech. **387**, 353 (1999).
[55] J. O. Smith, *Spectral Audio Signal Processing* (http://books.w3k.org, W3K Publishing, 2011).
[56] H. Sakamoto and H. Haniu, The formation mechanism and shedding frequency of vortices from a sphere in uniform shear flow, J. Fluid Mech. **287**, 151 (1995).
[57] L. Zeng, S. Balachandar, and P. Fischer, Wall-induced forces on a rigid sphere at finite reynolds number, J. Fluid Mech. **536**, 1 (2005).
[58] M. Ozgoren, E. Pinar, B. Sahin, and H. Akilli, Comparison of flow structures in the downstream region of a cylinder and sphere, Int. J. Heat Fluid Flow **32**, 1138 (2011).
[59] F. Noca, D. Shiels, and D. Jeon, A comparison of methods for evaluating time-dependent fluid dynamic forces on bodies, using only velocity fields and their derivatives, J. Fluids Struct. **13**, 551 (1999).